Optimal Aerodynamic Shape Design with Transition Prediction

by

Jonathan Driver

A thesis submitted in conformity with the requirements
for the degree of Masters of Applied Science
Graduate Department of Aerospace Engineering
University of Toronto

Abstract

Optimal Aerodynamic Shape Design with Transition Prediction

Jonathan Driver
Masters of Applied Science
Graduate Department of Aerospace Engineering
University of Toronto
2005

A two-dimensional Newton-Krylov aerodynamic shape optimization algorithm with laminar-turbulent transition has been developed. The coupled Euler and boundary-layer solver, MSES, is used to obtain transition locations, which are then used in the compressible Reynolds-Averaged Navier-Stokes (RANS) solver with the one-equation Spalart-Allmaras turbulence model. The sensitivity of the objective function to transition location perturbation is obtained from the RANS solutions. MSES is used to obtain the sensitivity of transition point movement to shape changes. These two sensitivities are combined to modify the discrete-adjoint objective function gradient. A unique design example demonstrates that the modified algorithm is able to design an airfoil very similar to one of the high-lift airfoils designed by Robert Liebeck. The design examples demonstrate that the optimizer is able to control the transition point locations to provide optimum performance, in effect designing optimized natural laminar-flow airfoils.

Acknowledgements

I would like to begin with thanking Professor David Zingg for his academic leadership, the enlightening conversations about industry and academic relationships, nurturing my curiosity, and being a constant source of motivation. I hope that I will be able to keep in close contact with his research group while I develop my career in the aeronautical industry. Professor Zingg attracts some of the most talented and well-rounded students that are interested in computational aerodynamics. For example, Marian Nemec, Todd Chisholm, Peterson Wong, Mohammad Tabesh, John Gatsis, and Jason Nichols. Each one of these individuals has helped me in some way to complete my degree.

The foundation of my thesis was laid down carefully by Marian Nemec. Marian, together with Professor Zingg, produced numerous well written research papers that provided a solid understanding of the fundamental approach to aerodynamic shape optimization. Near the end of my thesis Marian provided insightful suggestions into the last remaining issues and I am very grateful for his patience. Todd Chisholm also provided numerous suggestions about the challenges associated with linearizing the complete Spalart-Allmaras turbulence model in the Newton-Krylov framework. I am very thankful for his drive and determination to successfully achieve his research goals and help those around him achieve theirs. I would also like to thank Peterson, John, and Mohammad for all their support throughout my time at UTIAS. Peterson was always available to help me work out my issues and soothe the growing pains of graduate school. John entertained my curiosity with unique insights into alternate solutions to my problems. Mohammad demonstrated a careful and cautious approach to research that yields high quality work and a great deal of respect from his peers, especially me.

A very important person that certainly will never go without an acknowledgment is my good friend Jason Nichols. Jason has helped me succeed in my academic studies since the beginning of our undergraduate program back at the University of Alberta. I can not think of one situation over the past seven years that Jason did not achieve any of his goals. He has demonstrated to me what it takes to drive towards excellence and not settle for anything else other than perfection. I would like to thank him for all his support as both a colleague and as a good friend.

One of the most popular individuals to acknowledge in a thesis produced from the computational fluids research lab is Scott Northrup. Many of the frustrating moments in my two years at UTIAS were quickly diffused by Scott. I consider myself lucky on two fronts: firstly, that I graduated before Scott finished his tenure as system administrator of our research group, and secondly, that Scott became a valued colleague and a good friend.

To my family and friends. Thank you so very much. Without your unconditional support my degree was unobtainable.

Contents

List of Tables

List of Figures

List of Symbols

Alphanumeric Symbols

Δx_t grid spacing at the trip point

$\mathcal{J}$ objective function (scalar)

$\mathcal{X}$ design variable

a speed of sound

C constraint equations

c chord length of airfoil

C_D coefficient of drag

C_D^* target coefficient of drag

$C_f(x_i)$ coefficient of skin friction at airfoil location x_i

$C_f^*(x_i)$ target coefficient of friction at airfoil location x_i

C_L coefficient of lift

C_L^* target coefficient of lift

C_M coefficient of pitching moment

C_M^* target coefficient of pitching moment

C_P coefficient of pressure

C_P^* target coefficient of pressure

d distance to the closest wall

E inviscid flux in x-direction

e energy

E_v viscous flux in x-direction

F inviscid flux in y-direction

F_v viscous flux in y-direction

h finite-difference stepsize

$h(x_j)$ airfoil thickness at location x_j

J metric Jacobian

N number of nodes that violate the coefficient of friction constraint

p pressure

Q vector of conservative variables

R vector of discrete residual equations

S vorticity

T boundary layer transition location

u x-component of the velocity

v y-component of the velocity

x, y coordinates in the physical domain

x_{start}, x_{end} user defined boundary for coefficient of friction constraint

$\mathcal{P}r$ laminar Prandtl number

$\mathcal{P}r_t$ turbulent Prandtl number

Greek Symbols

α angle of attack

δ finite-difference stepsize for transition location perturbation

γ specific heat ratio

μ dynamic eddy viscosity

μ_t turbulent eddy viscosity

Ω MSES flow solution

ω_D user specified weight for the drag coefficient contribution to the objective function

ω_L user specified weight for the lift coefficient contribution to the objective function

ω_T user specified weight for thickness constraint contribution to the objective function

ω_{C_f} user specified weight for the coefficient of friction contribution to the objective function

ω_M user specified weight for the pitching moment coefficient contribution to the objective function

ρ density

Superscripts

$\bar{}$	dimensional variable
$\hat{}$	transformation to curvilinear coordinates
T	transpose

Subscripts

∞	freestream quantity
lo	lower surface
M	discrete variables for mean flow
T	discrete variable for turbulence model
up	upper surface

Chapter 1

Introduction

1.1 Motivation

The coupling of Computational Fluid Dynamics (CFD) with a numerical optimization process has demonstrated new and exciting ways of improving existing and future aircraft. From an aerodynamics standpoint it is desirable to have a process that will produce, or have the ability to produce, the most realistic results efficiently. This can be shown through the evolution of research codes over the past century. A number of excellent summaries of the progress in computational aerodynamics can be found in references [22, 31, 35, 64]. The results from the computed aerodynamics are in turn used to drive the optimization towards a solution that best suits the designers objectives. These objectives can be such things as reducing drag while improving lift, reducing drag while maintaining a constant lift, or producing families of non-inferior designs (Pareto fronts). The variety of objectives available allow the designer to explore a large design space effectively. Furthermore, being able to compute the aerodynamics accurately allows the optimization process to produce feasible designs.

The foundation on which this thesis is based, called Optima2D, was developed by Nemec and Zingg [36, 37]. The Newton-Krylov method is used to solve the two-dimensional fully turbulent Navier-Stokes equations. The objective function gradient is calculated using the discrete adjoint method. A quasi-Newton algorithm is used to minimize the objective function. The assumption of fully turbulent flow in the work of Nemec and Zingg eliminates the possibility of having a finite region of laminar flow existing on an airfoil, which is very probable for many different types of airfoils at various operating conditions. Extending the capability of allowing a finite region of laminar flow improves the fidelity of the computed aerodynamics. Exploiting the phenomenon of natural transition from laminar to turbulent flow in numerical optimization improves the

effectiveness of the optimization process. These two improvements provide a natural divide to this thesis. In the following section the first discussion will be focused on modeling laminar-turbulent transition in aerodynamics. The second discussion will focus on how to exploit this phenomenon in numerical optimization.

1.2 Background

1.2.1 Modeling Laminar-Turbulent Transition in Aerodynamics

Laminar-turbulent transition is considered one of most challenging research areas of aerodynamics. It has been widely accepted that transition in a boundary layer from smooth, steady flow (laminar) to fluctuating, agitated flow (turbulent) is caused by the growth of disturbances within the laminar boundary layer [3, 59]. Such flow disturbances can be caused by many sources, such as mechanical and acoustic vibrations, surface roughness, curvature, temperature, Mach number, and turbulence in the free-stream flow [14]. An excellent discussion about boundary layer instabilities can be found in Schlichting [44], while Van Dyke in his Album of Fluid Motion [13] contains superlative visual examples of various types of transition. More recently, Joslin has provided a comprehensive overview of work done in the area of laminar flow control from 1930's to the late 1990's [23]. Also, an excellent summary of recent transition analysis and prediction can be found in Herbert [19].

Before the National Aeronautics and Space Act of 1958 created NASA there existed NACA, the National Advisory Committee for Aeronautics. Between 1917 and 1958, NACA undertook exhaustive aeronautical experiments. During this period, especially the 1940's and 1950's, much of the research was focused on exploring transitional flows. Such experiments included studying the effects of boundary-layer transition on flat and curved plates and various NACA airfoil sections at various lift coefficients and Reynolds numbers [4, 6, 8, 28, 45, 46, 56]. As early as 1958, NACA undertook full-scale boundary-layer-flow visualization on the wings of a supersonic fighter airplane. The goal of this experiment was to better understand the boundary-layer flow at supersonic flight conditions [2]. Similar experiments were also conducted in 1999 at NASA Dryden to obtain data on the state of the boundary layer of natural laminar flow airfoil in supersonic flight [1]. The results of this experiment were later used to to provide accurate validation for Sturdza's design-orientated transition prediction routine for supersonic natural laminar airfoils [24, 53]. Almost 50 years after the 1958 full-scale supersonic boundary-layer-flow visualization experiment, the theories of transitional flows are still being tested. These examples are only a very small portion of the experiments conducted by NACA and NASA over the past

century. Numerous other research institutions have dedicated resources to studying transitional flows.

The difficulty with creating a unified transitional model is due to the inherent nature of transition itself. Researchers involved in exploring the transitional flow regimes make simplifying assumptions that allow for accurate modeling. As mentioned previously, several different factors affect the transition location. Currently, it is not possible to model all of the known effects on transition, although a few researchers are making significant gains [43]. Modeling transitional flows is a twofold process: modeling the physics of a transitional flow regime and finding the location of the transitional flow. The remaining part of this section will discuss popular methods of incorporating boundary-layer transition into aerodynamic computations.

A common method for numerical incorporating the physics of turbulence into aerodynamics calculations is via a turbulence model. Godin and Zingg [16] successful implemented the one-equation Spalart-Allmaras [48] and Menter SST [33] turbulence model into the Navier-Stokes computation for high-lift aerodynamic flows. Each of the models showed various levels of accuracy in different operating conditions and airfoil configurations. The method of determining where the transition location occurred was through comparison to experimental data, and the transition location is fixed accordingly. Each of the turbulence models uses empirical relationships to represent the destruction, production, diffusion and advection of eddy viscosity throughout the flow regime. One of the results from Godin and Zingg's work was that the Spalart-Allmaras model was best suited for mildly separated flows. Although the Spalart-Allmaras model does not automatically predict the transition location, the model does allow for transitional flows. The transition location is usually determined from experimental measurements or rules of thumb.

Another popular method is to couple the Euler equations with a boundary-layer solver. The boundary layer solutions represent the viscous components of the aerodynamics that the Euler equations miss. Since the boundary-layer information, such as the shape factor and momentum thickness, is easily obtained from this approach, the ability to predict the transition location based on this information is also easily implemented. This is an advantage that the Euler/boundary-layer solvers have over the RANS approach. An effective and popular way of dealing with transition is by modeling an envelope tuned to the boundary layer instability frequencies, shape factors and Reynolds number momentum thicknesses. This method is called the e^N envelope method, which is based on linear stability theory [47, 55]. Drela incorporated this method into the popular two-dimensional Euler/boundary-layer solver called MSES [12]. Drela eventually went on to couple the solver with an optimization process with success in 1993 [10]. Recently, Sturdza extended the design-oriented transition prediction capabilities to be

three-dimensional. The success of the Euler/boundary-layer method has spurred motivation to incorporate the similar type of prediction capabilities to the RANS equations. Recent success has shown that coupling the e^N method into a Navier-Stokes code proves a significant challenge [5, 49, 50, 51, 52].

An alternative approach that has been gaining popularity over the past decade has been to include transition components directly into existing turbulence models. An advantage with this approach is that the model is based on local variables which makes the implementation into a RANS solver fairly straight forward. The results from this approach have demonstrated similar results are obtained when compared to e^N boundary-layer methods [21, 25, 26, 34, 54, 62, 57, 58]. A major drawback to this approach is the massive amount of empiricism that is used to develop the models themselves. Not only does the onset of transition need to be modeled, so does the evolution of laminar to turbulent flow. Langtry and Menter [25] recently developed an approach where the evolution of laminar to turbulent flow is modeled with an intermittency transport equation that basically adjusts the level of turbulent viscosity throughout the flow field. The onset of transition is modeled via another transport equation based on the Reynolds number momentum thickness. Those two models determine where transition will occur and how turbulence develops. Similar to many turbulence models, this model will also require calibration. In terms of using this approach as a design tool in numerical optimization, a significant challenge will be in formulating the components required for effective aerodynamics optimization.

This leads into the next subsection which will discuss using transition prediction methods in the design of airfoils via an optimization process and introduce a few of the associated research challenges.

1.2.2 Transition Prediction as a Design Tool

The current work extends from Nemec and Zingg, who coupled a fully turbulent RANS flow solver with an aerodynamic shape optimization process and demonstrated the advantages of approaching the design problem using a Newton-Krylov algorithm [36, 37]. The method in which Nemec calculated the aerodynamic shape gradients was by finite difference, discrete adjoint, and the flow sensitivity approach (originally developed in the Newton-Krylov frame work by Wong [61]). The default method of computing the gradient is the discrete adjoint. It is desirable to maintain this method of computing the gradient since it is independent of the number of design variables. It is at this point that two challenges appear. The first is the extension of the fully turbulent RANS flow solver to have laminar-turbulent transition

prediction capabilities. The second is to determine a method in which the impact on the objective function from the movement of the transition location is known in the calculation of the discrete adjoint gradient. This is rarely done at present and provides the motivation for this research. The remaining discussion in this section will focus on what work has been done in aerodynamic optimization assuming a region of laminar flow.

In 1993 Dodbele developed an optimization method to design axisymmetric body shapes in subsonic compressible flow [9]. The aerodynamic analysis is carried out with an inviscid analysis. The pressure distribution from this analysis is used in the boundary-layer solver. At each station the boundary-layer stability equations are solved. Finally, the transition location is predicted with the e^N method. The computation of the objective function, the maximization of the upper and lower transition locations, is carried out at this step. Finally the objective function gradient is calculated using the simplified Granville's transition criterion. Granville in 1953 introduced a boundary-layer transition criterion for axisymmetric boundary layers applied to bodies of revolution; basically a curve fit based on the difference between the momentum thickness Reynolds number and the neutral point versus an average pressure gradient parameter [17]. Using a simplified transition criterion, Dodbele argued, is required to avoid the expense of computing the objective function gradient based on the e^N method. The objective is constrained through the use of geometric and aerodynamic constraints. The method was used in the design of an axisymmetric tip-tank for a business-jet. The use of Granville's method to calculate the objective function gradient forces the method to be confined to axisymmetric problems.

In 1996 Green et al. developed an optimization method for the constrained design of natural laminar flow airfoils [18]. Similar to Dodbele, the pressure distribution over an initial airfoil is computed using an Euler solver. The pressure distribution is passed into a boundary-layer solver to obtain velocity and temperature profiles. The velocity and temperature profiles are then used to obtain boundary layer stability information (N-factors) at specified stations along the airfoil. From this information a target N-factor distribution is imposed, presumably formulated by the designer. Once this step is complete, a target pressure distribution is calculated that results in convergence towards the specified N-factor distribution. The target pressure distribution in the recovery region is formed from a weighted average of the initial pressure recovery region, and a linear scaling of the initial pressure recovery region based on the coefficient of pressure at 70% chord. Once the upper surface target pressure is modified to meet the aerodynamic constraints, further modifications are required to meet the leading-edge constraints. This iterative design cycle is repeated until a specified convergence criterion is met. The method was used in the design of natural laminar flow airfoils. Green et al. demonstrated improved re-designs of already

existing natural laminar airfoils. The range of Mach and Reynolds numbers presented were 0.10 and 3 million to 0.60 and 20 million. This method required a significant amount of user know-how into specifying appropriate N-factor distributions, and understanding the influence of pressure recovery regions on boundary layer instability.

In 2003 Pralits developed an optimization method applied to natural and hybrid laminar flow control on wings using solutions of the adjoint equations to obtain the objective function gradients [40]. The optimization method was applied to laminar flow control for both passive (wing shape) and active devices (suction). Only passive laminar flow control will be discussed here. In order to formulate the objective function gradient based on the adjoint method, Pralits formed a composite gradient based on three different governing equations: the steady compressible Euler equations, the steady boundary layer equations, and the parabolized stability equations. The adjoint equations for each of the three governing equations are solved separately and combined. The gradient is used in a quasi-Newton algorithm to minimize the objective function. A composite objective function which includes the disturbance kinetic energy, pressure drag and penalties on the deviations of lift and pitching moment coefficients. Pralits was able to capture the effects of natural transition due to laminar instability via the analysis of three different governing equations and form an objective function gradient from three different adjoint formulations. The methodology was tested in the design of wings for natural laminar flow. Pralits demonstrated that an efficient method to minimize boundary layer disturbances is to formulate the adjoint based on the stability equations themselves.

In 2004 Sturdza developed an optimization method to design natural laminar flow wings for use in supersonic flight [24, 53]. Sturdza uses information from the Euler solution to obtain viscous information via a compressible boundary-layer solver. The e^N envelope method is used to determine the transition location and is based on Drela's work. Modifications to include cross-flow instabilities and compressibility effects were developed. Sturdza also uses the more accurate finite-difference approach to obtain the boundary-layer solution while Drela used the integral method. The objective function used in the optimization is based on the instability envelope of the boundary layers. A number of optimization strategies were applied in finding an optimum solution in a design space where possible discontinuities exist: sequential quadratic programming (SQP), the Nelder-Mead simplex algorithm, a genetic algorithm, and response-surface trust region methods. Sturdza uses the complex-step method to compute the gradients required for the SQP method, and demonstrated that the complex-step method filtered the noise from the viscous drag computation, thus providing accurate gradients. The method was used to investigate the trade-offs between viscous and inviscid drag for supersonic natural laminar flow wing/body configurations. A number of interesting results were obtained from Sturdza's work.

The formulation of the objective function made the design space very noisy since the growth or decay of the instabilities are very non-linear. This caused the gradient based methods to fail on converging towards a local optimum. The result was that the gradient-free methods provided an improved robustness to navigating the design space. Although the objective function and methodology of obtaining the aerodynamic characteristics in Sturdza's work is very different for those presented in this thesis, he demonstrated a significant challenge associated with coupling a transition prediction routine with an optimization process applied to supersonic aircraft. The highly non-linear characteristics of the laminar-turbulent transition can cause problems with effectively navigating the design space.

The above four examples display the sparsity of past research that has been done in aerodynamic optimization assuming a region of laminar flow exists. The room for improvement in this area of research is incredible. Improvements are required in being able to capture the physics of boundary layer transition and using optimization techniques to minimize an objective function incorporating a transition criterion. Furthermore, the above four examples were all developed using an Euler/boundary-layer flow solver to calculate the aerodynamic coefficients. As mentioned at the beginning of this section, the current work extends from a fully turbulent compressible RANS flow solver, which is rarely done at present.

1.3 Objectives

The research objective is to develop a laminar-turbulent transition prediction routine into a two-dimensional aerodynamic optimization that will allow the manipulation of the transition locations. In order to achieve this objective, the following research milestones must be reached:

- Incorporate the trip terms of the Spalart-Allmaras (SA) turbulence model into the Newton-Krylov flow solver contained in Optima2D
- Incorporate a routine into the flow solver that will obtain accurate transition locations
- Investigate and resolve issues involving free transition movement during the optimization cycle

Chapter 2

Governing Equations

A natural way to divide the current chapter is into two sections of discussion: aerodynamic shape optimization and the equations that govern aerodynamic flows. The first part of this chapter, aerodynamic shape optimization, provides the majority of the details required to solve the aerodynamic optimization problem. The remaining details can be found in Nemec [36]. The second part of this chapter, aerodynamic flow equations, deals with the Reynolds-Averaged Navier-Stokes (RANS) equations, the Spalart-Allmaras turbulence model and the e^N envelope transition prediction methodology.

2.1 Aerodynamic Shape Optimization

2.1.1 Problem Formulation

The formulation of the optimization problem begins with presenting a minimization of the objective function $\mathcal{J}$ with constraints $\mathcal{C}$. The result is the design variables $\mathcal{X}$ that satisfy the minimization problem. Presented in its mathematical form:

$$\min_{\mathcal{X}} \mathcal{J}(\mathcal{X}, Q) \tag{2.1}$$

subject to:

$$C_j(\mathcal{X}, Q) \leq 0 \qquad j = 1, ..., N_c \tag{2.2}$$

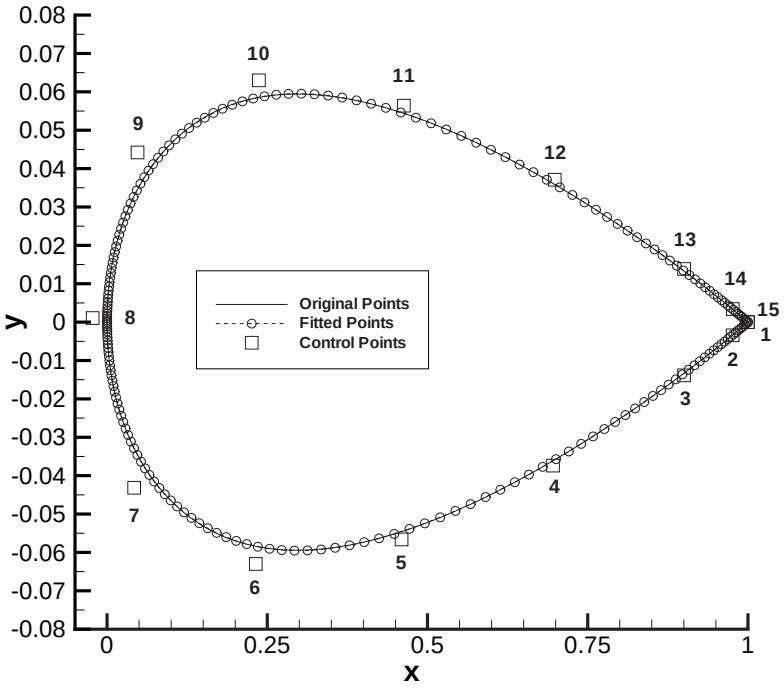

Figure 2.1: B-spline curve and control points for the NACA 0012 airfoil

where Q contains the flow variables, and N_c is the number of constraint equations imposed. Furthermore, the flow-field variables must satisfy the flow equations in the flow-solver. This allows the optimizer to know how the change in the design variables, and ultimately the change in the shape of the airfoil, will affect the flow solution.

2.1.2 Design Variables

The design variables are specified control points from fitting a B-spline to the airfoil surface. Changing the number of control points is an option if the optimization design requires more control over certain areas of the airfoil. Nemec only evaluated the vertical displacements of the control points. An example of a NACA 0012 is shown in Figure 2.1. An additional design variable can be found in allowing the angle of attack, α, to change during the optimization cycle.

2.1.3 Objective Functions

Nemec evaluated numerous objective functions, for example:

1) maximization of the lift-to-drag ratio,

$$\mathcal{J} = \frac{C_L}{C_D} \tag{2.3}$$

2) lift-constrained drag minimization,

$$\mathcal{J} = \omega_D(1 - C_D/C_D^*)^2 + \omega_L(1 - C_L/C_L^*)^2 \tag{2.4}$$

where C_D^* and C_L^* represent target drag and lift coefficients, while ω_D and ω_L are user defined constants, and

3) inverse design,

$$\mathcal{J} = \frac{1}{2}\sum_{j=1}^{N_\mathrm{A}}(C_{\mathrm{p}_j} - C_{\mathrm{p}_j}^*)^2 \tag{2.5}$$

Hua et al. [20, 29], recently provided an additional objective function of:

4) endurance factor maximization,

$$\mathcal{J} = \frac{C_L^{3/2}}{C_D} \tag{2.6}$$

Each of the above objective functions are examined later in Chapter 5. In Section 5.5 a composite objective function that is used to maximize lift, as well as constraining the pitching moment and skin friction coefficient will be introduced.

2.1.4 Constraints

The optimization is formulated as an unconstrained problem. In order to accomplish this Nemec combined the constraint equation into the objective function using a penalty method:

$$\mathcal{J} = \mathcal{J}_O + \mathcal{J}_G \tag{2.7}$$

where $\mathcal{J}_O$ is the objective function, equation 2.3 for example, and $\mathcal{J}_G$ is the geometrical constraints. A variety of geometrical constraints are possible. For example, the penalty method

based on the minimum allowable thickness of the airfoil can be expressed using a quadratic penalty term.

$$h^*(x_j) - h(x_j) \leq 0 \tag{2.8}$$

h^* represents the minimum allowable thickness at location x_j and $h(x_j)$ represents the current thickness. When this constraint is active, the value is added to the objective function. This addition "penalizes" the objective function for the violation. Other geometrical constraints are an area constraint and a floating thickness constraint.

2.1.5 Gradient Calculation

Discrete Adjoint

The gradient of the objective function, $\mathcal{J}$, is calculated using the discrete-adjoint method:

$$\frac{d\mathcal{J}}{d\mathcal{X}} = \frac{\partial \mathcal{J}}{\partial \mathcal{X}} - \psi^T \frac{\partial R}{\partial \mathcal{X}} \tag{2.9}$$

where R is the residual vector of the discretized flow equations. The above equation describes the change of the objective function relative to a change in the design variables based on the sensitivity of objective and residual functions. The adjoint equation, which is independent of the design variables and only based on the flow variables, is solved for the vector ψ:

$$\frac{\partial R^T}{\partial Q}\psi = \frac{\partial \mathcal{J}^T}{\partial Q} \tag{2.10}$$

In order to solve for ψ, Nemec [36] used the GMRES method. $\frac{\partial \mathcal{J}}{\partial \mathcal{X}}$ and $\frac{\partial R}{\partial \mathcal{X}}$ are solved using centered-differencing.

Since the Spalart-Allmaras turbulence model does not automatically predict the transition location, the sensitivity information of the objective function with respect to perturbations in the transition locations is not included in equation 2.9. Under certain conditions the location of transition from laminar to turbulent flow can have a significant effect on aerodynamic performance, especially drag. Under these conditions it is important to allow the optimization algorithm to manipulate the transition point through shape changes. The following sub-section is designated for this discussion.

Modified Discrete Adjoint

In order to provide the gradient with information about how the movement of the transition location will affect the objective function, we modify the discrete adjoint, given in equation 2.9, in the following manner:

$$\frac{d\mathcal{J}}{d\mathcal{X}} = \frac{\partial \mathcal{J}}{\partial \mathcal{X}} - \psi^T \frac{\partial R}{\partial \mathcal{X}} + \frac{\partial \mathcal{J}}{\partial \mathcal{T}} \frac{\partial \mathcal{T}}{\partial \mathcal{X}} \tag{2.11}$$

Where the sensitivity of the objective function with respect to the transition location movement $\frac{\partial \mathcal{J}}{\partial \mathcal{T}}$ is combined, via the chain rule, with the movement of the transition location due to airfoil perturbations $\frac{\partial \mathcal{T}}{\partial \mathcal{X}}$. This product contains the contribution of the upper and lower transition location sensitivities, which are denoted by the subscripts "up" and "lo" below:

$$\frac{\partial \mathcal{J}}{\partial \mathcal{T}} \frac{\partial \mathcal{T}}{\partial \mathcal{X}} = \frac{\partial \mathcal{J}}{\partial T_{lo}} \frac{\partial T_{lo}}{\partial \mathcal{X}} + \frac{\partial \mathcal{J}}{\partial T_{up}} \frac{\partial T_{up}}{\partial \mathcal{X}} \tag{2.12}$$

A finite-difference approximation of the $\frac{\partial \mathcal{J}}{\partial \mathcal{T}}$ term is used for both the upper and lower airfoil surfaces, given by

$$\frac{\partial \mathcal{J}}{\partial T_{lo}} = \frac{\mathcal{J}\left[\mathcal{X}, Q(\mathcal{X}, T_{lo} + \delta)\right] - \mathcal{J}\left[\mathcal{X}, Q(\mathcal{X}, T_{lo} - \delta)\right]}{2\delta} \tag{2.13}$$

$$\frac{\partial \mathcal{J}}{\partial T_{up}} = \frac{\mathcal{J}\left[\mathcal{X}, Q(\mathcal{X}, T_{up} + \delta)\right] - \mathcal{J}\left[\mathcal{X}, Q(\mathcal{X}, T_{up} - \delta)\right]}{2\delta} \tag{2.14}$$

where δ is the grid spacing surrounding the trip node. This guarantees that the perturbation of the transition location moves by 1 grid node.

The terms $\frac{\partial T_{up}}{\partial \mathcal{X}}$ and $\frac{\partial T_{lo}}{\partial \mathcal{X}}$ are found via finite differences of airfoil perturbations using MSES, given by

$$\frac{\partial T\left(T_{up}, T_{lo}\right)}{\partial \mathcal{X}} = \frac{T\left[\Omega(\mathcal{X} + h)\right] - T\left[\Omega(\mathcal{X} - h)\right]}{2h} \tag{2.15}$$

where

$$h = \max\left(\epsilon \cdot |\mathcal{X}|, 1 \times 10^{-5}\right) \tag{2.16}$$

A typical value of ϵ is 1×10^{-3}, and the smallest value of h is limited to 1×10^{-5} to avoid gradient inaccuracies with small stepsizes. It is important to note that equations 2.13 and 2.14 require a new RANS flow solve for each perturbed state, while equation 2.15 requires one MSES flow solve per design variable perturbation.

2.1.6 Optimizer

The unconstrained problem is solved using the Broyden-Fletcher-Goldfarb-Shanno (BFGS) quasi-Newton algorithm in conjunction with a backtracking line search. The goal of the optimizer is to reduce the norm of the gradient vector to zero, thereby reaching a local minimum for the design problem. The quasi-Newton algorithm determines a search-direction vector at each iteration of the optimizer. Once the search-direction is determined, it updates the design variables using a line-search procedure. It is instructive to note that the search-direction vector is solved using the inverse of the Hessian matrix multiplied by the gradient vector of the objective function. Nemec mentions that the calculation of the exact Hessian matrix is not practical and therefore the BFGS secant update is used to generate a series of matrices that approximate the inverse of the exact Hessian matrix with increasing accuracy. As mentioned above, the update of the design variables uses a line-search procedure. Nemec implemented a backtracking line-search procedure that finds an acceptable value of the stepsize used to update the design variables.

2.2 Aerodynamic Flow Equations

The flow equations that govern two-dimensional aerodynamic flows with reasonable accuracy are the Reynolds-averaged thin-layer Navier-Stokes equations. This section is dedicated to describing them in their partial differential form. The following chapter explains how the partial differential form is discretized to form ordinary differential equations (ODE's). A time marching method is applied to the ODE's to obtain ordinary difference equations (OΔE's). Within this section it is not the intention to describe the entire methodology of how we solve the Navier-Stokes equations. Rather, the focus of this section is on the components that were modified to help achieve the thesis objectives. When applicable, the remaining details will be noted as references.

2.2.1 Navier-Stokes Equations

The conservative variables that are being solved for are

$$Q = \begin{bmatrix} \rho \\ \rho u \\ \rho v \\ e \end{bmatrix} \tag{2.17}$$

The steady-state equations in two-dimensional Cartesian coordinates are

$$\frac{\partial E}{\partial x} + \frac{\partial F}{\partial y} = \mathcal{R}e^{-1}\left(\frac{\partial E_v}{\partial x} + \frac{\partial F_v}{\partial y}\right) \tag{2.18}$$

The inviscid fluxes are

$$E = \begin{bmatrix} \rho u \\ \rho u^2 + p \\ \rho uv \\ (e+p)u \end{bmatrix}, \quad F = \begin{bmatrix} \rho v \\ \rho vu \\ \rho v^2 + p \\ (e+p)v \end{bmatrix} \tag{2.19}$$

The viscous fluxes are

$$E_v = \begin{bmatrix} 0 \\ \tau_{xx} \\ \tau_{xy} \\ E_{v,4} \end{bmatrix}, \quad F_v = \begin{bmatrix} 0 \\ \tau_{xy} \\ \tau_{yy} \\ F_{v,4} \end{bmatrix} \tag{2.20}$$

with the stress terms

$$\begin{aligned} \tau_{xx} &= (\mu + \mu_t)(4u_x - 2v_y)/3 \\ \tau_{xy} &= (\mu + \mu_t)(u_y - v_x)/3 \\ \tau_{yy} &= (\mu + \mu_t)(-2u_x + 4v_y)/3 \\ E_{v,4} &= u\tau_{xx} + v\tau_{xy} + (\mu\mathcal{P}r^{-1} + \mu_t\mathcal{P}r_t^{-1})(\gamma-1)^{-1}\partial_x(a^2) \\ F_{v,4} &= u\tau_{xy} + v\tau_{yy} + (\mu\mathcal{P}r^{-1} + \mu_t\mathcal{P}r_t^{-1})(\gamma-1)^{-1}\partial_y(a^2) \end{aligned} \tag{2.21}$$

where μ and μ_t are the viscosity and turbulent eddy viscosity.

2.2.2 Turbulence Model

Modeling complex phenomena, such as turbulence, is an acceptable method to reduce the computational requirements and still capture the physics. A popular turbulence model is the Spalart-Allmaras one-equation model [48], which is solved for the turbulent eddy viscosity, ν_t.

The development of the Spalart-Allmaras turbulence model came from an empirical approach to approximate, term by term, a transport equation for the turbulent eddy viscosity. A new term was generated after each additional physical effect was considered. Godin et al. [16] showed that the Spalart-Allmaras turbulence model is an effective model for attached and mildly separated aerodynamic flows.

The one-equation Spalart-Allmaras turbulence model equation is:

$$\frac{D\tilde{\nu}}{Dt} = c_{b1}[1 - f_{t2}]\tilde{S}\tilde{\nu} + \frac{1 + c_{b2}}{\sigma}\nabla \cdot [(\nu + \tilde{\nu})\nabla\tilde{\nu}] - \frac{c_{b2}}{\sigma}(\nu + \tilde{\nu})\nabla^2\tilde{\nu} - \left[c_{w1}f_w - \frac{c_{b1}}{\kappa^2}f_{t2}\right]\left(\frac{\tilde{\nu}}{d}\right)^2 + f_{t1}\Delta U^2 \tag{2.22}$$

The first term on the right hand side of the equation 2.22 is the production term, the second and third are diffusion terms, the fourth is the destruction term and the fifth is the trip term.

The turbulent eddy viscosity is given by

$$\nu_t = \tilde{\nu} f_{v1} \tag{2.23}$$

where:

$$f_{v1} = \frac{\chi^3}{\chi^3 + c_{v1}^3} \tag{2.24}$$

$$\chi = \frac{\tilde{\nu}}{\nu} \tag{2.25}$$

The modified vorticity, $\tilde{S}$ in the production term is given by

$$\tilde{S} = S + \frac{\tilde{\nu}}{\kappa^2 d^2} f_{v2} \tag{2.26}$$

where S is the magnitude of the vorticity, d is the distance to the closest wall, and

$$f_{v2} = 1 - \frac{\chi}{1 + \chi f_{v1}} \tag{2.27}$$

The destruction function f_w is

$$f_w = g\left[\frac{1 + c_{w3}^3}{g^6 + c_{w3}^6}\right]^{\frac{1}{6}} \tag{2.28}$$

$$g = r + c_{w2}(r^6 - r) \tag{2.29}$$

$$r = \frac{\tilde{\nu}}{\tilde{S}\kappa^2 d^2} \tag{2.30}$$

Transition is incorporated using the two functions f_{t1} and f_{t2}. The first one is the source term in the region of the trip points, while the latter tends to bring small values of $\tilde{\nu}$ to zero. This helps to ensure that transition only occurs near the trip point.

The equations are

$$f_{t1} = c_{t1} g_t \exp(-c_{t2}\frac{\omega_t^2}{\Delta U^2}[d^2 + g_t^2 d_t^2]) \tag{2.31}$$

$$f_{t2} = c_{t3} \exp(-c_{t4}\chi^2) \tag{2.32}$$

The factor g_t ensures that the trip term is non-zero over at least a few nodes. It is defined as

$$g_t = \min\left(0.1, \frac{\Delta U}{\omega_t \Delta x_t}\right) \tag{2.33}$$

where d_t is the distance to the trip point, ω_t is the vorticity at the trip point, and Δx_t is the grid spacing at the trip point. ΔU is the velocity difference between the point at which the

equation is being calculated and the trip point. The remaining constants are

$$\begin{aligned} c_{b1} &= 0.1355 & c_{b2} &= 0.622 \\ c_{t1} &= 5.0 & c_{t2} &= 10.0 \\ c_{t3} &= 1.2 & c_{t4} &= 0.5 \\ c_{w1} &= c_{b1}/\kappa^2 + (1 + c_{b2})/\sigma & & \\ c_{w2} &= 0.3 & c_{w3} &= 2.0 \\ c_{v1} &= 7.1 & & \\ \sigma &= \tfrac{2}{3} & \kappa &= 0.41 \end{aligned} \tag{2.34}$$

The remaining details of the coordinate transformation from Cartesian to generalized curvilinear coordinates and the thin-layer approximation can be found in Pulliam [42]. An excellent description of the grid metrics and boundary conditions can be found in Pueyo [41].

In order to determine accurate transition locations, the MSES Euler/boundary-layer code is used. As mentioned in the background section of this thesis, MSES uses the e^N envelope method to predict when the laminar instabilities produced from Tollmien-Schlichting waves will most likely produce boundary layer transition. Further details of this method can be found in Drela et al. [12].

Chapter 3

Algorithm Description

Similar to Chapter 2, this chapter is also divided into two natural sections of discussion: flow analysis and optimization. The first part of this chapter, flow analysis, will discuss modifications to the flow analysis algorithm. The second part of this chapter, optimization, will discuss modifications to the discrete-adjoint gradient algorithm. The original algorithms of flow analysis and the discrete gradients can found in Nemec [36].

3.1 Flow Analysis

In order to solve the Navier-Stokes equations and the Spalart-Allmaras turbulence model equations described in Section 2.2, they must be transformed into a system of ordinary difference equations (OΔE's). The first step is to approximate the spatial derivatives by using finite-differences. A useful reference to finite-difference approximations applied to CFD applications can be found in [30]. For steady flows, the result is a system of nonlinear algebraic equations. The next and final step in the process is to solve this system via an implicit Newton-Krylov method using an approximate factorization algorithm to start-up.

3.1.1 Spatial Discretization

The spatial discretization of the governing equations is the same as used in ARC2D [42] for structured C-topology applications. All the grids presented in this thesis are generated with AMBER2D [60]. The details of the discretization of the inviscid and viscous fluxes, the artificial-dissipation operators, boundary conditions can be found in Nemec [36]. These have not been modified in the current work. The production and destruction terms in the Spalart-Allmaras

turbulence model were modified to allow for laminar-turbulent flow regimes. A brief description of the model in the steady-state form will be discussed here.

The complete Spalart-Allmaras turbulence model in steady-state form, rewritten for convenience and clarity purposes, takes the following form

$$J^{-1}\left[M(\tilde{\nu}) - P(\tilde{\nu}) + D(\tilde{\nu}) - N(\tilde{\nu})\right] = 0 \tag{3.1}$$

where

$$M(\tilde{\nu}) = U\frac{\partial\tilde{\nu}}{\partial\xi} + V\frac{\partial\tilde{\nu}}{\partial\eta} \qquad \text{convective term} \tag{3.2}$$

$$P(\tilde{\nu}) = \frac{c_{b1}}{\mathcal{R}e}\tilde{S}\tilde{\nu}\left(1 - f_{t2}\right) + \mathcal{R}e f_{t1}\Delta U^2 \qquad \text{production term} \tag{3.3}$$

$$D(\tilde{\nu}) = \left(\frac{c_{w1}f_w}{\mathcal{R}e} - \frac{c_{b1}f_{t2}}{\kappa^2\mathcal{R}e}\right)\left(\frac{\tilde{\nu}}{d_{\mathrm{w}}}\right)^2 \qquad \text{destruction term} \tag{3.4}$$

$$N(\tilde{\nu}) = \frac{1}{\sigma\,\mathcal{R}e}\left[\left(1 + c_{b2}\right)T_1 - c_{b2}T_2\right] \qquad \text{diffusion term} \tag{3.5}$$

The factor of J^{-1} is introduced to improve the scaling of the flow Jacobian matrix. It is important to note that the Spalart-Allmaras turbulence model does not predict the transition location. The trip term, $\mathcal{R}e f_{t1}\Delta U^2$, acts as a source for the evolution of turbulent growth in the boundary layer. The discretization of equation 3.1 was unmodified from the fully turbulent version.

3.1.2 Flow Solver

The spatial discretization of the governing equations leads to the following nonlinear system of equations:

$$R(\widehat{Q}, \mathcal{X}) = 0 \tag{3.6}$$

where $\widehat{Q}$ represents the discrete flow variables.

A solution to equation 3.6 can be found by applying Newton's method:

$$\frac{\partial R^{(n)}}{\partial \widehat{Q}^{(n)}} \Delta \widehat{Q}^{(n)} = -R^{(n)} \tag{3.7}$$

A preconditioning matrix is applied from the right side

$$\frac{\partial R}{\partial \widehat{Q}} M^{-1} M \Delta \widehat{Q} = -R \tag{3.8}$$

The preconditioning matrix is based on the first-order approximation to the flow Jacobian. An equivalent system is solved using matrix-free generalized minimal residual (GMRES) method. Since GMRES does not require the explicit formation of $\frac{\partial R}{\partial \widehat{Q}}$, it is approximated using first-order forward differencing.

In order to incorporate the changes in the Spalart-Allmaras model, the 5×5 blocks within the approximate flow Jacobian must be modified. The terms that require modification are $\frac{\partial R_{\mathrm{T}}}{\partial \widehat{Q}_{\mathrm{M}}}$ and $\frac{\partial R_{\mathrm{T}}}{\partial \widehat{Q}_{\mathrm{T}}}$ shown below,

$$\begin{pmatrix} \begin{bmatrix} \\ \frac{\partial R_{\mathrm{M}}}{\partial \widehat{Q}_{\mathrm{M}}} \\ 4 \times 4 \\ \\ \end{bmatrix} & \begin{bmatrix} \\ \frac{\partial R_{\mathrm{M}}}{\partial \widehat{Q}_{\mathrm{T}}} \\ 4 \times 1 \\ \\ \end{bmatrix} \\ \begin{bmatrix} \\ \frac{\partial \mathbf{R}_{\mathrm{T}}}{\partial \widehat{\mathbf{Q}}_{\mathrm{M}}} \\ 1 \times 4 \\ \\ \end{bmatrix} & \begin{bmatrix} \frac{\partial \mathbf{R}_{\mathrm{T}}}{\partial \widehat{\mathbf{Q}}_{\mathrm{T}}} \\ 1 \times 1 \end{bmatrix} \end{pmatrix} \tag{3.9}$$

where the contributions from the flow variables, $\widehat{Q}_{\mathrm{M}}$, and the Navier-Stokes residual, R_{M}, are clearly distinguished from the turbulence model variables, $\widehat{Q}_{\mathrm{T}}$, and the Spalart-Allmaras residual, R_{T}.

At this point it should be noted that the trip function, $\mathcal{R}ef_{t1}\Delta U^2$, found in the production term of equation 3.5 does not need to be included in the flow Jacobian that is used to form the preconditioner for the system, equation 3.9, and only exists on the right hand side of equation 3.8. Chisholm showed that the added differentiation of this trip function only slightly

affects convergence [7]. In Section 4.3.1 the importance of linearizing to improve gradient accuracy is explored.

Before solving equation 3.8 the transition locations are obtained from a complete MSES solution. This is done in order to eliminate the computational expense of coupling a boundary-layer transition routine, such as the e^N method, with a RANS solve, which was thoroughly discussed in Section 1.2.1. Therefore a "flow solve" requiring transition prediction requires one MSES solution followed by one RANS solution.

3.2 Optimization

Modifications to the original optimization algorithm in Optima2D were made in the calculation of the discrete adjoint gradient. This section will describe in detail how the gradient was modified in a step-by-step approach. To aid in this discussion a flow chart of the computational steps involved in forming the modified discrete adjoint gradient, equation 2.11, will be presented.

3.2.1 Modified Discrete-Adjoint Gradient

As mentioned in Section 2.1.5, the original discrete adjoint required modifications to provide the gradient with information about how the movement of the transition location will affect the objective function.

The following flow chart is intended to act as a road map for how the components making up the discrete adjoint are calculated.

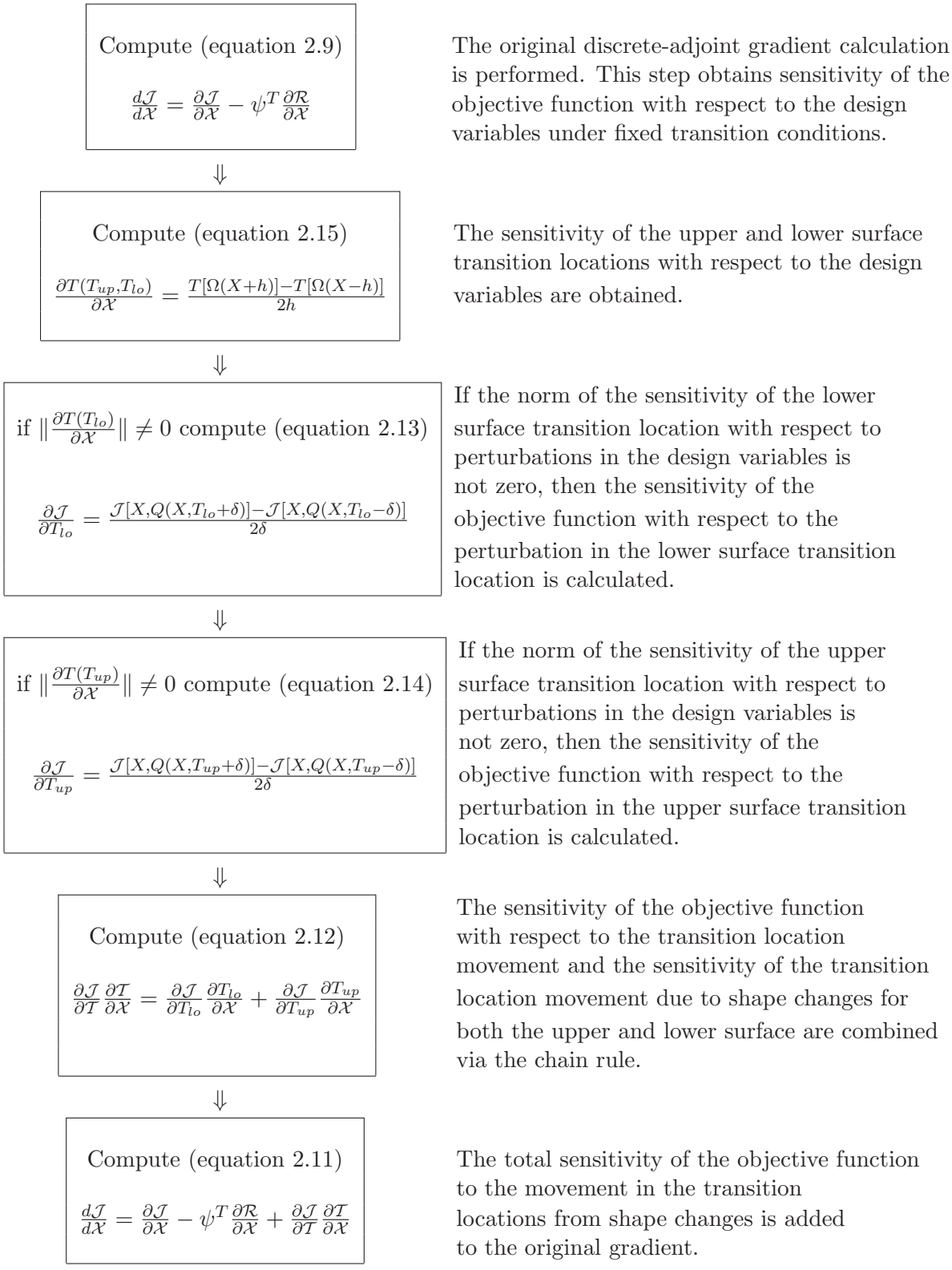
Compute (equation 2.9)
$\frac{d\mathcal{J}}{d\mathcal{X}} = \frac{\partial \mathcal{J}}{\partial \mathcal{X}} - \psi^T \frac{\partial \mathcal{R}}{\partial \mathcal{X}}$
The original discrete-adjoint gradient calculation is performed. This step obtains sensitivity of the objective function with respect to the design variables under fixed transition conditions.
⇓
Compute (equation 2.15)
$\frac{\partial T(T_{up},T_{lo})}{\partial \mathcal{X}} = \frac{T[\Omega(X+h)]-T[\Omega(X-h)]}{2h}$
The sensitivity of the upper and lower surface transition locations with respect to the design variables are obtained.
⇓
if $\|\frac{\partial T(T_{lo})}{\partial \mathcal{X}}\| \neq 0$ compute (equation 2.13)
$\frac{\partial \mathcal{J}}{\partial T_{lo}} = \frac{\mathcal{J}[X,Q(X,T_{lo}+\delta)]-\mathcal{J}[X,Q(X,T_{lo}-\delta)]}{2\delta}$
If the norm of the sensitivity of the lower surface transition location with respect to perturbations in the design variables is not zero, then the sensitivity of the objective function with respect to the perturbation in the lower surface transition location is calculated.
⇓
if $\|\frac{\partial T(T_{up})}{\partial \mathcal{X}}\| \neq 0$ compute (equation 2.14)
$\frac{\partial \mathcal{J}}{\partial T_{up}} = \frac{\mathcal{J}[X,Q(X,T_{up}+\delta)]-\mathcal{J}[X,Q(X,T_{up}-\delta)]}{2\delta}$
If the norm of the sensitivity of the upper surface transition location with respect to perturbations in the design variables is not zero, then the sensitivity of the objective function with respect to the perturbation in the upper surface transition location is calculated.
⇓
Compute (equation 2.12)
$\frac{\partial \mathcal{J}}{\partial \mathcal{T}} \frac{\partial \mathcal{T}}{\partial \mathcal{X}} = \frac{\partial \mathcal{J}}{\partial T_{lo}} \frac{\partial T_{lo}}{\partial \mathcal{X}} + \frac{\partial \mathcal{J}}{\partial T_{up}} \frac{\partial T_{up}}{\partial \mathcal{X}}$
The sensitivity of the objective function with respect to the transition location movement and the sensitivity of the transition location movement due to shape changes for both the upper and lower surface are combined via the chain rule.
⇓
Compute (equation 2.11)
$\frac{d\mathcal{J}}{d\mathcal{X}} = \frac{\partial \mathcal{J}}{\partial \mathcal{X}} - \psi^T \frac{\partial \mathcal{R}}{\partial \mathcal{X}} + \frac{\partial \mathcal{J}}{\partial \mathcal{T}} \frac{\partial \mathcal{T}}{\partial \mathcal{X}}$
The total sensitivity of the objective function to the movement in the transition locations from shape changes is added to the original gradient.

Chapter 4

Validation

4.1 Overview

This chapter will discuss the performance of the presented algorithm. The first section, Flow-Solver Performance, will demonstrate the performance of the Newton-Krylov algorithm with the trip terms in the Spalart-Allmaras turbulence model. This section will also explore the feasibility of using MSES to obtain accurate transition locations prior to the RANS solution. The second section, Gradient Accuracy, will discuss the accuracy of the gradient under fixed and free boundary layer transition. The details of the operating conditions, grid and geometric parameterization are presented for each test case.

4.2 Flow-Solver Performance

4.2.1 AF-NK

An approximately-factored algorithm, Cyclone, is used to validate the modifications to the Spalart-Allmaras turbulence model in the Newton-Krylov flow solver. The complete Spalart-Allmaras turbulence model was originally developed and validated in Cyclone by Godin and Zingg [16]. Nemec implemented the fully turbulent version of the Spalart-Allmaras model in the Newton-Krylov flow solver, using the fully turbulent formulation of the model in Cyclone as start-up. The present algorithm now uses the complete model in Cyclone as start-up and the complete model in the Newton-Krylov flow solver.

The GA(W)-1 [32], LNV109A [39], NACA-0012 and ZINGG-1981 [63] airfoils are chosen to

Case	Airfoil	Dimensions	Points on airfoil	Off-wall spacing ($\times 10^{-6}$)	Leading-edge clustering ($\times 10^{-3}$)	Trailing-edge clustering ($\times 10^{-3}$)
A	GA(W)-1	265x53	201	2.0	2.0	2.0
B	LNV109A	389x65	325	1.0	0.1	0.1
C	NACA-0012	284x65	220	1.0	0.1	0.1
D	ZINGG-1981	289x65	225	1.0	0.1	0.1

Table 4.1: Grid details for Cases A, B, C and D

Case	Mach Number	Angle of Attack	Reynolds Number (10^6)	T_{up} (x/c)	T_{lo} (x/c)
A	0.25	4.00	2.00	19.91	67.40
B	0.25	9.00	5.00	27.47	95.17
C	0.25	2.00	1.00	44.27	85.53
D	0.25	1.93	1.00	73.16	94.99

Table 4.2: Operating conditions for Cases A, B and C

evaluate the Newton-Krylov algorithm and the transition prediction method. The four different airfoils on four different structured C-grids are tested to insure the presented modifications to the algorithm do not penalize the robustness of the flow solver. Tables 4.1 and 4.2 describe the grids and operating conditions used to evaluate the performance of the flow solver for single element airfoils.

For all cases, the preconditioner constant is set to 6.0 and the level of fill is set to 2. These are identical to the values used in the fully turbulent cases presented by Nemec [36]. Figure 4.1 demonstrates that the Newton-Krylov (NK) flow solver with approximate-factorization (AF) start-up is three to five times faster than a complete solution with AF. Table 4.3 shows the coefficients of lift (C_L) and drag (C_D) obtained from the AF-NK flow solve for **Cases A**, **B**, **C**, and **D**. Identical values are achieved to machine precision from a complete AF flow solve.

Two internally generated MSES grids used to obtain the transition locations for **Cases B** and **D** are shown in Figure 4.2. Table 4.4 lists the details of the grid parameters used to generate the

Case	Coefficient of Lift (C_L)	Coefficient of Drag (C_D)(10^{-2})
A	0.8779	1.413
B	1.466	1.453
C	0.2207	0.7024
D	0.8884	1.0672

Table 4.3: Coefficients of lift (C_L) and drag (C_D)

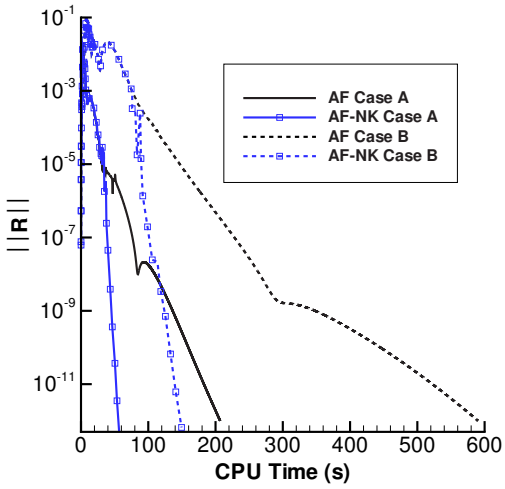

Figure 4.1: Performance of the Newton-Krylov flow solver for Cases A and B

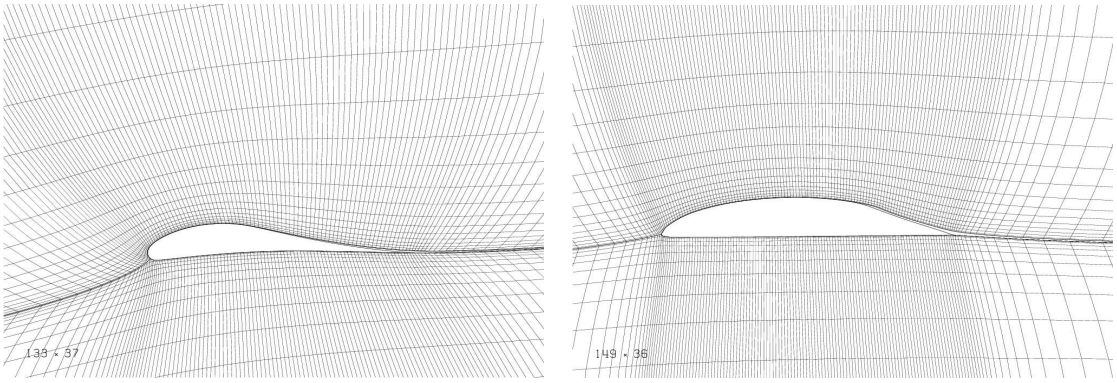

(a) Case B (b) Case D

Figure 4.2: MSES grids for Case B and Case D

grids used in **Cases B** and **D**. The grid parameters listed are similar to case studies performed by Giles and Drela [11, 15], and are considered good quality grids. The letters N, E, I, O, T, B, X and A correspond to MSES input parameters.

4.2.2 MSES Versus AF-NK

As mentioned in Section 3.1.2, MSES is used to obtain the transition locations prior to the RANS flow solve. Therefore it is important that the pressure distribution from the Euler/boundary-layer solution produced matches the pressure distribution produced from the RANS solution. Figure 4.3 shows the similarity between the MSES and RANS pressure distributions for all the

	Case B	Case D
Dimensions	138x37	149x36
Airfoil side points (N)	82	110
Exponent for airfoil side points (E)	1.0	0.4
Inlet points on leftmost airfoil streamline (I)	26	20
Outlet points on rightmost airfoil streamline (O)	26	20
Number of streamlines in top of domain (T)	20	21
Number of streamlines in bottom of domain (B)	17	15
X-spacing parameter (X)	0.50	0.85
Aspect ratio of each cell at stagnation point (A)	2.50	2.50

Table 4.4: MSES grid details for Case B and Case D

cases described in Table 4.2. Obtaining the boundary-layer transition locations prior to the RANS solve seems to be reasonably acceptable, with the ZINGG-1981 airfoil showing the worst similarity between the MSES and RANS solutions.

4.2.3 Warm Starting

The method of warm starting was used by Nemec to elevate the flow solver time and greatly speed-up the convergence of the optimizer. During a line search Nemec used the converged flow solution from the last optimization iteration as the initial conditions, rather than starting over from free stream conditions. The dangers involved with warm starting are small under fully turbulent conditions but are significant with laminar-turbulent conditions. In order to demonstrate the problems with warm starting a solution under laminar-turbulent conditions, the following numerical experiment is performed. **Case C** is used, with an additional 5 grid points added to the airfoil surface, as the test case with various upper transition locations listed in Table 4.5. The lower surface transition location is fixed throughout the experiment. Initially a series of flow solutions are performed starting from free stream conditions. The results from these flow solutions are shown in Table 4.5 under the "free stream" heading. These solutions are then compared with warm starting each solution with the the furthest downstream transition

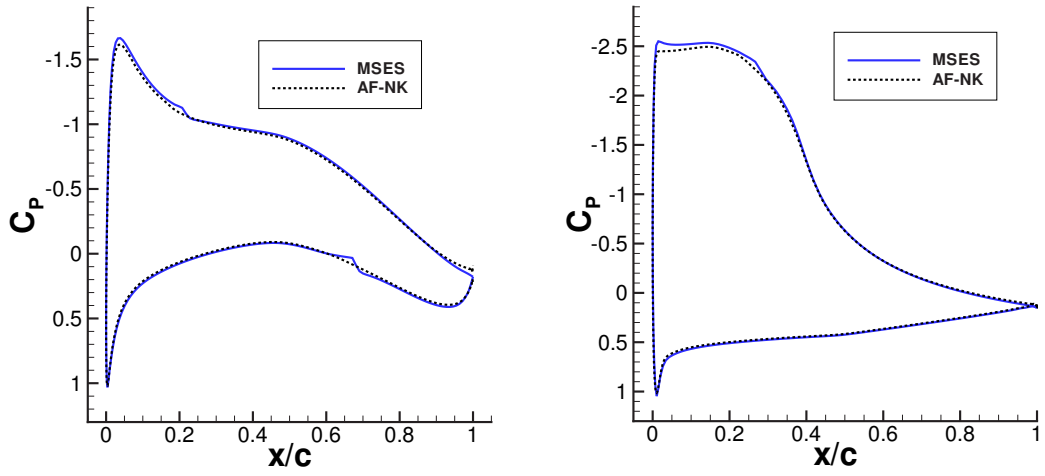

(a) Case A

(b) Case B

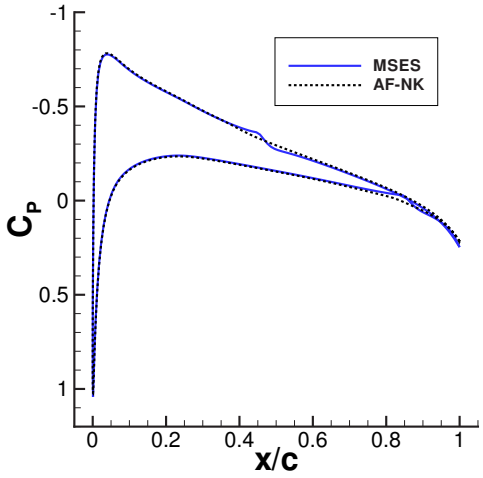

(c) Case C

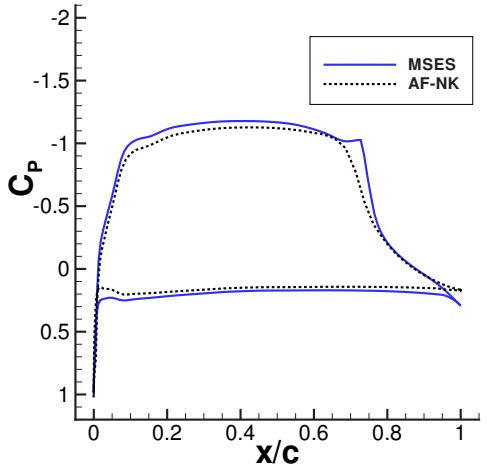

(d) Case D

Figure 4.3: Euler/boundary-layer solutions versus RANS solutions for Cases A, B, C and D

	Free Stream		Warm Start	
T_{up} (x/c)	Coefficient of Lift (C_L)	Coefficient of Drag $(C_D)(10^{-2})$	Coefficient of Lift (C_L)	Coefficient of Drag $(C_D)(10^{-2})$
44.27	0.2207	0.7024	0.2207	0.7024
40.96	0.2194	0.7175	0.2205	0.7038
37.72	0.2180	0.7326	0.2180	0.7326
34.57	0.2167	0.7477	0.2153	0.7627
31.54	0.2153	0.7628	0.2153	0.7628

Table 4.5: Effect of warm starting a solution under laminar-turbulent conditions: Case C

	Free Stream		Warm Start	
T_{up} (x/c)	Coefficient of Lift (C_L)	Coefficient of Drag $(C_D)(10^{-2})$	Coefficient of Lift (C_L)	Coefficient of Drag $(C_D)(10^{-2})$
31.54	0.2153	0.7628	0.2153	0.7628
34.57	0.2167	0.7477	0.2153	0.7627
37.72	0.2180	0.7326	0.2153	0.7627
40.96	0.2194	0.7175	0.2153	0.7627
44.27	0.2207	0.7024	0.2153	0.7627

Table 4.6: Effect of warm starting a solution under laminar-turbulent conditions: Case C

location; in this particular case the location was 44.27%. The results from this experiment are shown in Table 4.5 under the "warm start" heading.

A similar experiment is performed to the one described above, except in reverse order. The transition location is moved downstream with warm starting from the furthest upstream transition location; in this particular case the location was 31.54%. The results from this experiment are shown in Table 4.6

As shown in Table 4.5, the highly non-linear nature of the turbulence model trip functions, Equations 2.31 and 2.32, cause non-unique turbulent growth. Furthermore, as shown in Table 4.6, nodes that are turbulent will not become laminar. These experiments demonstrate dangerous scenarios when dealing with laminar-turbulent conditions, not only with the possibility of converging towards two different solutions but also forming a gradient based on the perturbation in the transition location, Equations 2.13 and 2.14. The result from this experiment prohibits the use of warm starting the flow solves during the optimization process, in both the calculation of the objective function and the formation of the gradient.

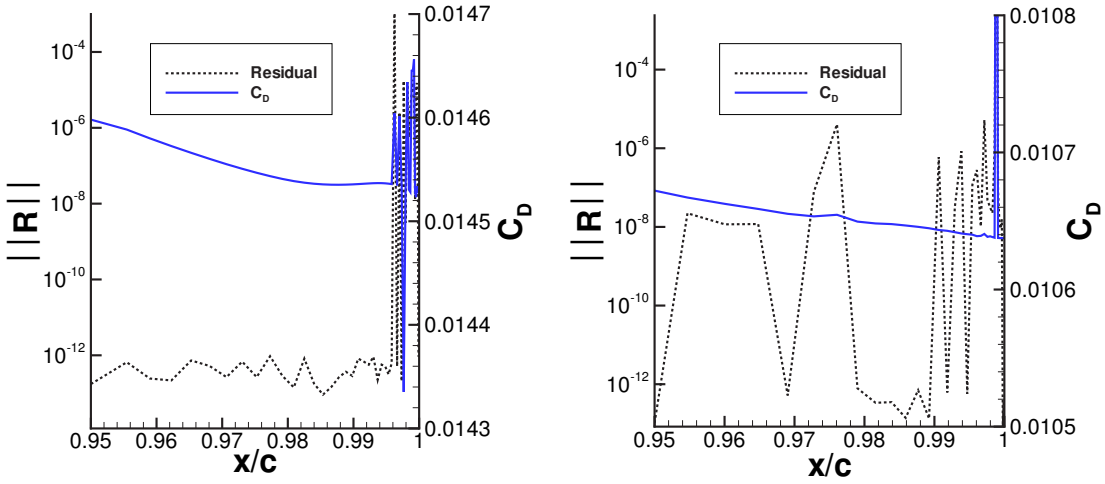

(a) Case B (b) Case D

Figure 4.4: Lower surface transition location constraint

4.2.4 Lower Surface Transition Location Constraint

Many of the airfoils studied in this thesis experience laminar flow over the entire lower surface. The probability of successfully converging the RANS flow solver to near machine zero is reduced when the lower surface transition location is near the trailing edge. A good example of this can be demonstrated using **Cases B** and **D** described in Tables 4.1 and 4.2. The lower surface transition point is incremented, node by node, from approximately 95% chord to 100% chord. At each increment the RANS solution residual is required to converge beyond 10^{-12}. The results from this experiment are shown in Figure 4.4. The RANS flow solver experiences convergence issues when the lower surface transition location exceeds 99% chord and 95% chord for **Cases B** and **D**, respectively. Poorly converged solutions can lead to inaccurate gradients and can confuse the line search algorithm. Therefore it is necessary to constrain the lower surface transition location a "safe" distance from the trailing edge. A "safe" distance implies that it is up to the user's discretion. The "safe" distance can vary depending on, for example, grid resolution near the trailing edge, operating conditions, and turbulence model coefficients.

4.3 Gradient Accuracy

This section will discuss the gradient accuracy of the modified discrete adjoint gradient, Equation 2.11. The first subsection will discuss the accuracy of the modified discrete adjoint gradient with fixed transition locations, Equation 2.9. The second subsection will discuss the accuracy of the individual components making up the modified discrete adjoint gradient, Equation 2.11.

4.3.1 Fixed Transition

Nemec evaluated the gradient accuracy of the discrete adjoint formulation relative to the finite-difference gradient under fully turbulent conditions. We follow the same method of evaluation for the gradient accuracy under fixed transition conditions. The airfoil, grid, operating conditions, and objective function are identical, except under laminar-turbulent conditions, to Nemec's gradient accuracy validation for the subsonic inverse design problem (case 1). The finite-difference stepsize constant is set to 1×10^{-5}. This particular case is revisited since the gradient evaluation via finite-differences remains constant for a range of stepsizes. This property allows for a reasonable amount of confidence in the accuracy of the finite-difference calculation, which is used to evaluate the accuracy of the adjoint gradient calculation. The fixed transition locations on the upper and lower surface are 22.41% chord and 95.00% chord, respectively.

The evaluation of the discrete-adjoint gradient under fixed transition conditions is done in four steps. The first step is to evaluate the accuracy of the gradient without linearizing the trip term, Equation 2.31. The second step is to evaluate the gradient accuracy due to the linearization of the trip term into the second order Jacobian. The third step is to evaluate the gradient accuracy due to the linearization of the trip distance term, d_t in Equation 2.31, in $\frac{\partial R}{\partial \mathcal{X}}$ of Equation 2.9. The fourth and final step is to examine the influence of combined linearizing the trip term, f_{t1}, and trip distance term, d_t, in the overall gradient accuracy. The results are shown in Table 4.7. A small error is experienced in the adjoint gradients relative to the finite-difference gradients. The lowest error occurs when the linearization of d_t in $\frac{\partial R}{\partial \mathcal{X}}$ is combined with the linearization of the trip term, f_{t1}. From this experiment the linearization of d_t and f_{t1} are used in the calculation of the gradient under fixed transition conditions.

4.3.2 Free Transition

The trip terms in the Spalart-Allmaras turbulence model are based on the airfoil surface distributions of the grid nodes. The corresponding transition location is forced to exist at a surface

Table 4.7: Gradient accuracy for case C: Fixed transition

Control Point #	Finite Difference	Adjoint[a] (% Diff.)	Adjoint[b] (% Diff.)	Adjoint[c] (% Diff.)	Adjoint[d] (% Diff.)	S-MF[e] (% Diff.)
9	-0.120540E+03	-0.0174	-0.0166	-0.0174	-0.0166	0
10	0.567582E+03	0.0026	0.0026	0.0026	0.0026	0
11	-0.195382E+04	-0.0194	-0.0097	-0.0189	-0.0097	0
12	-0.493992E+03	-0.0198	-0.0198	-0.0192	-0.0192	-0.0022

[a] unmodified
[b] linearization of the trip term f_{t1} in second-order Jacobian
[c] linearization of d_t in $\frac{\partial R}{\partial \mathcal{X}}$
[d] combined linearization of f_{t1} and d_t
[e] matrix-free flow-sensitivity

node. Although perturbations in the airfoil shape will perturb the transition location, the movement may not be significant enough to force the transition location onto another node. This makes it impossible to evaluate the modified discrete-adjoint gradient using the approach described in Section 4.3.1 above. Instead we evaluate the accuracy of individual components making up the modified discrete-adjoint gradient, specifically, $\frac{\partial \mathcal{J}}{\partial \mathcal{T}}$ and $\frac{\partial \mathcal{T}}{\partial \mathcal{X}}$.

Objective Function Sensitivity due to Transition Location Perturbation

The sensitivity of $\frac{\partial \mathcal{J}}{\partial \mathcal{T}}$ contains contributions from the upper, $\frac{\partial \mathcal{J}}{\partial T_{up}}$, and lower, $\frac{\partial \mathcal{J}}{\partial T_{lo}}$, surfaces. The evaluation of the sensitivity of these two components is fairly straightforward. For example, to evaluate $\frac{\partial \mathcal{J}}{\partial T_{up}}$ the upper surface transition location is perturbed upstream and/or downstream, guaranteeing the transition location has moved by a one grid node for each perturbation, while keeping the lower surface transition location, T_{lo}, fixed. A similar process is repeated for $\frac{\partial \mathcal{J}}{\partial T_{lo}}$. It is important to note that each time the transition location moves, a RANS solve, starting from free stream conditions, is required (see Section 4.2.3). The sensitivity of $\frac{\partial \mathcal{J}}{\partial \mathcal{T}}$ is evaluated using the grid and operating conditions listed in Tables 4.8 and 4.9 for the NACA 0012 airfoil. The off-wall spacing, leading-edge clustering, and trailing-edge clustering for all the grids listed in Table 4.8 are identical to **Case C** listed in Table 4.1. A couple of points are worth mentioning to help understand the results presented in this subsection. First, since our objective function is based on the aerodynamic coefficients, such as C_L and C_D, the sensitivity analysis only concerns these coefficients; the sensitivity of a specific objective function can be derived from them. Second, the x-axis in Figures 4.5 and 4.5 uses a sign convention of moving transition upstream, towards the leading edge, as negative, and downstream, towards the trailing edge, as positive. Furthermore the values on the x-axis are relative to the transition location based

Case	Dimensions	Points on airfoil
G1	239x65	175
G2	289x65	225
G3	339x65	275
G4	389x65	325
G5	439x65	350

Table 4.8: Grid details for the NACA 0012 $\frac{\partial \mathcal{J}}{\partial \mathcal{I}}$ evaluation cases

Case	Mach Number	Angle of Attack	Reynolds Number (10^6)
OP1	0.25	2.00	1.00

Table 4.9: Operating condition for the NACA 0012 $\frac{\partial \mathcal{J}}{\partial \mathcal{I}}$ evaluation cases

on the closest grid node to the transition locations obtained from a converged MSES solution.

Figure 4.5 shows that, qualitatively speaking, the sensitivity, or slope, of the objective function due to the perturbation in the transition location is relatively smooth. Therefore, reasonable confidence in the gradient can be obtained using first-order forward, first-order backward, and second-order centered differences. The second-order centered difference is more accurate than the first order approximations, which is expected, but the penalty is that it requires two additional flow solutions. Furthermore, basing the perturbation on the neighboring grid node spacing to the transition location node is acceptable for a wide range of grid spacings. This last point is based on the observation that the slopes of the line remain fairly similar over the different mesh sizes. Table 4.10 quantitatively assesses the accuracy of the first-order forward, first-order backward, and second-order centered difference approximations to the sensitivity of C_L and C_D for case G2-OP1.

The error associated with the sensitivity of C_L and C_D due to the transition location movement is largely dependent on the grid node spacing surrounding the transition location. Since we are using highly stretched cells on the surface of the airfoil to save some computational

Order	$\frac{\partial C_L}{\partial T_{up}}$	$\frac{\partial C_D}{\partial T_{up}}$	$\frac{\partial C_L}{\partial T_{lo}}$	$\frac{\partial C_D}{\partial T_{lo}}$
1^{st} order forward	0.0357	-0.0047	0.0543	0.0023
1^{st} order backward	0.0383	-0.0047	0.0396	0.0027
2^{nd} order centered	0.0374	-0.0047	0.0466	0.0025

Table 4.10: Sensitivity of C_L and C_D with respect to the upper and lower surface transition location movement for case G2-OP1

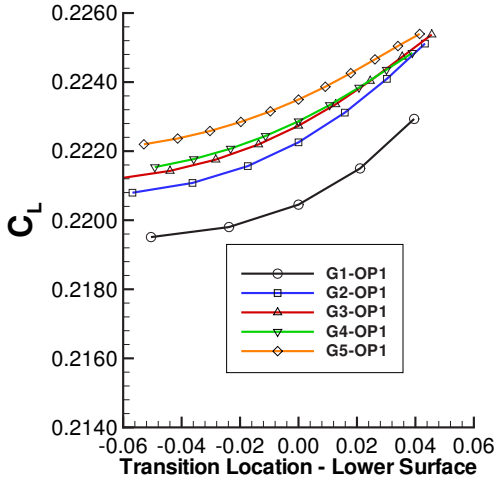

(a) Sensitivity of $\frac{\partial C_L}{\partial T_{lo}}$

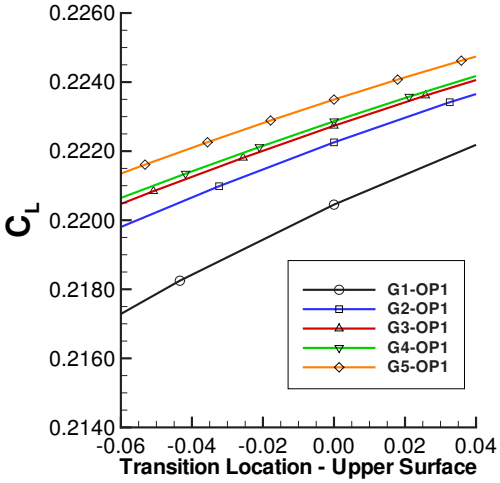

(b) Sensitivity of $\frac{\partial C_L}{\partial T_{up}}$

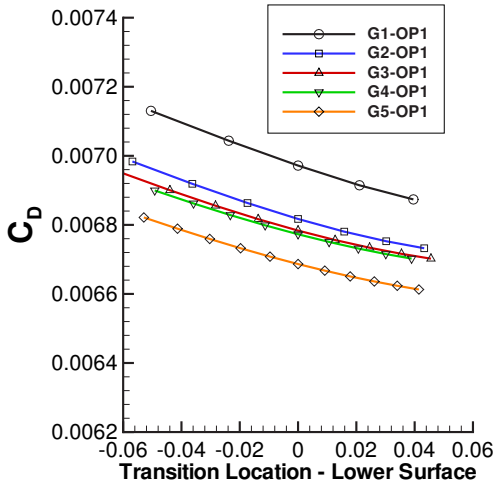

(c) Sensitivity of $\frac{\partial C_D}{\partial T_{lo}}$

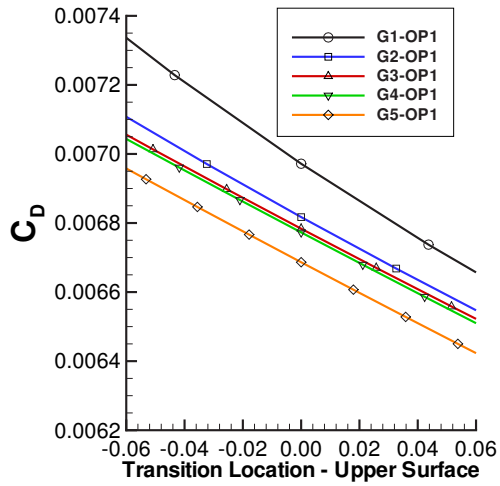

(d) Sensitivity of $\frac{\partial C_D}{\partial T_{up}}$

Figure 4.5: Sensitivity of C_L and C_D with respect to transition location movement

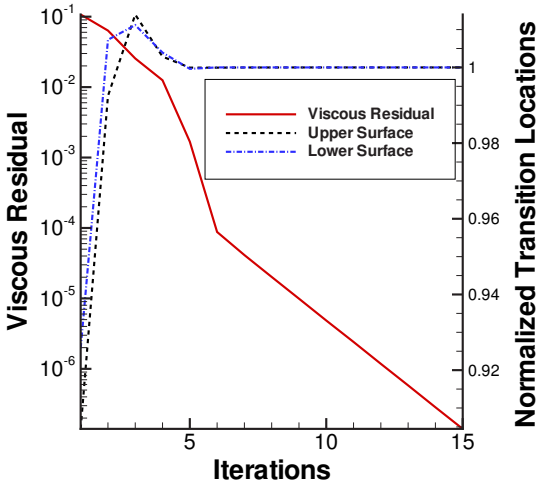

Figure 4.6: Convergence of the upper and lower transition locations associated with the overall viscous residual of MSES

effort, we sacrifice being able to discretize the sensitivity of C_L and C_D due to transition location movement to a high level of accuracy. Although a level of gradient inaccuracy is present, the methodology of obtaining the transition locations via an Euler/boundary-layer solution is probably a worse approximation. Therefore, in terms of reducing the computational expense of obtaining the $\frac{\partial \mathcal{J}}{\partial \mathcal{T}}$ term, the first-order approximations allow for reasonably accurate sensitivities at a low cost. First-order backward difference is the default method in which to obtain approximate the $\frac{\partial \mathcal{J}}{\partial \mathcal{T}}$ term.

Transition Location Sensitivity due to Design Variable Perturbation

The sensitivity of $\frac{\partial \mathcal{T}}{\partial \mathcal{X}}$ contains contributions from the upper, $\frac{\partial T_{up}}{\partial \mathcal{X}}$, and lower surface, $\frac{\partial T_{lo}}{\partial \mathcal{X}}$. Since the transition locations are obtained from MSES, which can be considered a black box, the input is the airfoil shape, angle of attack and operating conditions while the output is the transition locations. Both the $\frac{\partial T_{up}}{\partial \mathcal{X}}$ and $\frac{\partial T_{lo}}{\partial \mathcal{X}}$ terms are calculated for each design variable perturbation simultaneously. Each perturbation requires a complete converged MSES solution. Since the transition location values are used to form a gradient, confidence in these values is paramount. In order to eliminate as much error in the calculation of this term as possible, the viscous residual in MSES is reduced to 10^{-6}. From numerical experiments, the transition locations have converged beyond eight significant digits. Figure 4.6 demonstrates the convergence of the transition locations associated with the overall viscous residual for **Case C** listed in Table 4.2.

A major challenge associated with obtaining $\frac{\partial \mathcal{T}}{\partial \mathcal{X}}$ is choosing a stepsize, ϵ in Equation 2.16.

In order to examine the behaviour of $\frac{\partial T}{\partial \mathcal{X}}$ a range of various ϵ values are tested. **Case C** is parametrized with 12 design variables, specifically design variables 2-7 and 9-14 shown in Figure 2.1. The angle of attack is also included as the 13th design variable. Figure 4.7 illustrates the range of stepsizes and the corresponding sensitivity values for each design variable.

Since the stepsize is scaled with the design variables, as shown in Equation 2.16, extremely small stepsizes are possible. This leads to inaccurate sensitivity values, which may lead to large errors in the gradient calculation. In order to avoid inaccurate sensitivity values the scaled stepsizes are required to be greater than or equal to 1×10^{-5}. This constraint avoids possible errors associated with small stepsizes, which are shown in Figure 4.7(b).

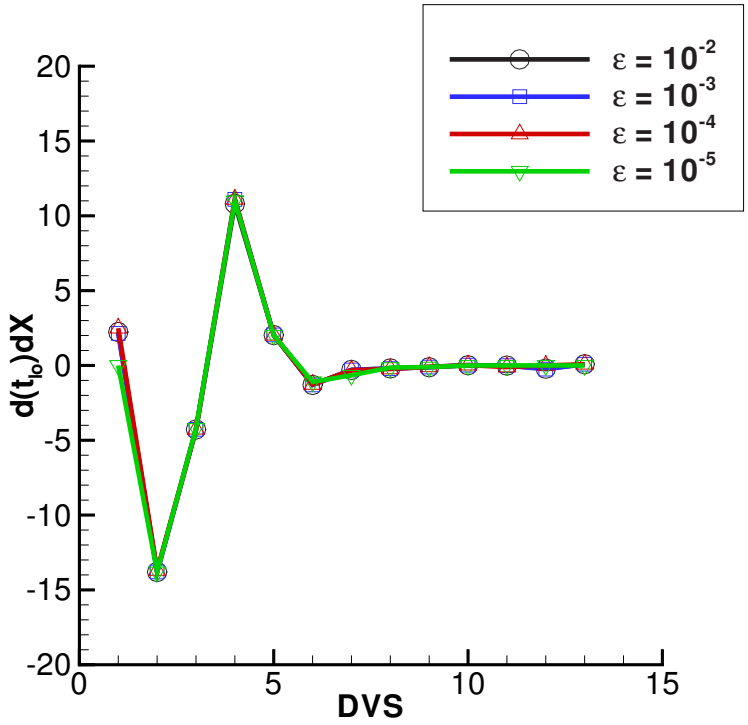

(a) Lower surface

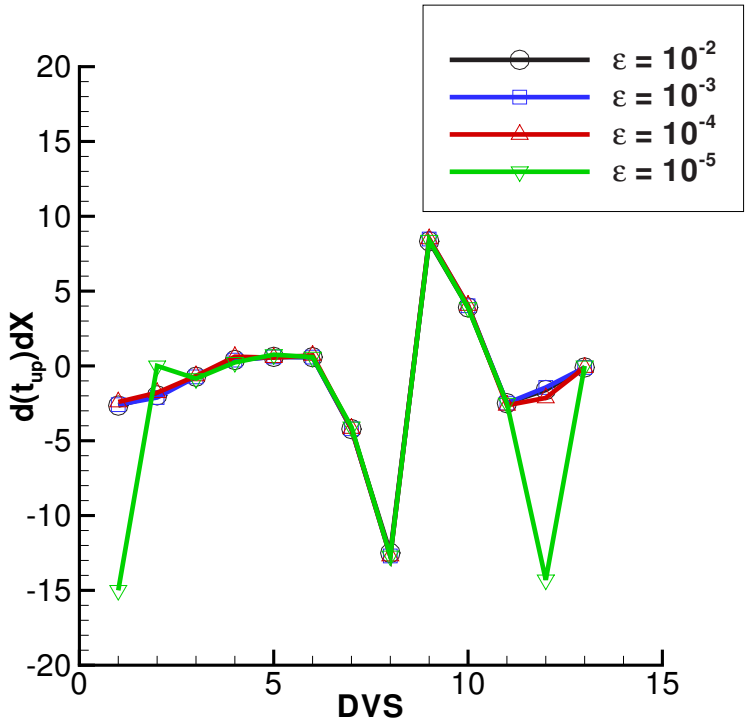

(b) Upper surface

Figure 4.7: Sensitivity of the upper and lower transition locations due to shape changes with various stepsizes

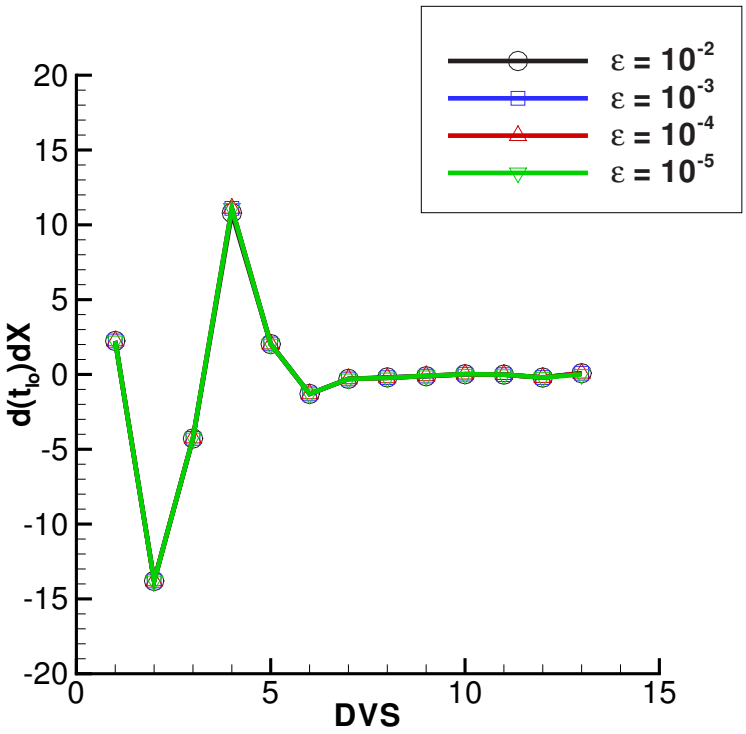

(a) Lower surface

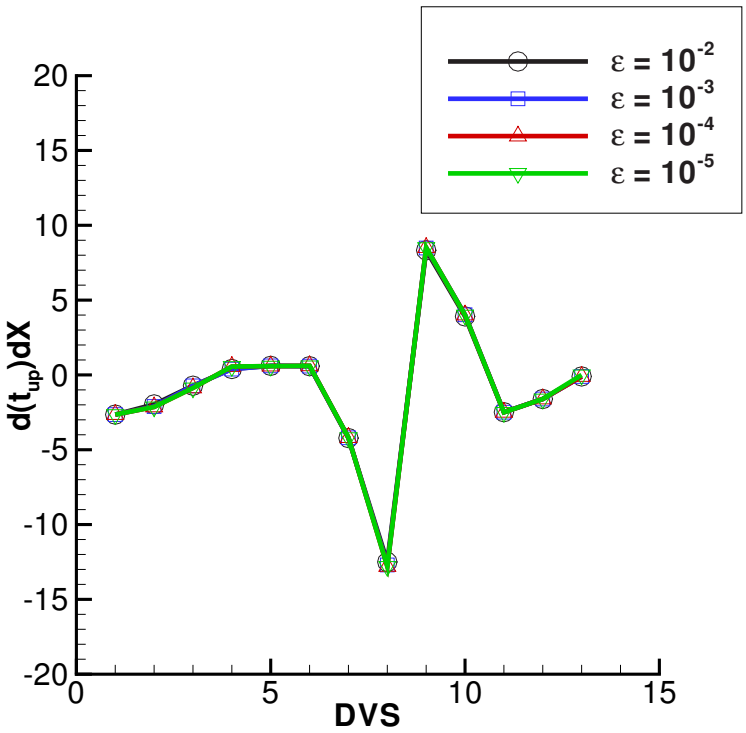

(b) Upper surface

Figure 4.8: Sensitivity of the upper and lower transition locations due to shape changes with a minimum tolerance on the allowable stepsize

Chapter 5

Design Examples

5.1 Overview

This chapter will present design examples using the proposed methodology. Each design section is sub-divided into individual case studies, which are listed numerically to clearly distinguish them from the cases used in Chapter 4. The first paragraph in each subsection will describe or refer to the grid used in the design, the airfoil parameterization, and the operating conditions. The subsequent paragraphs will discuss the results from the case study. This chapter is used as an avenue to explore the advantages and disadvantages of performing shape optimization with the proposed transition prediction routine and modified gradient evaluation.

5.2 Maximization of the Lift-to-Drag Ratio

The maximization of the lift-to-drag ratio, Equation 2.3, of four cases is presented in this section.

Case 1: Mach Number = 0.25, Reynolds Number = 1 million

Case 1 uses the grid described for **Case C** in Table 4.1, and is designed at a Mach number of 0.25 and a Reynolds number of 1 million. The initial angle of attack is set to 2 degrees. The NACA 0012 airfoil is parameterized using 15 B-spline control points, of which 12 are used as design variables, and the locations are indicated in Figure 2.1. Control points 2-7 are used as design variables on the lower surface, with control points 9-14 used as design variables on the

Table 5.1: Lift-to-drag ratio maximization: Case 1

Case	$\frac{C_L}{C_D}$	C_L	C_D	T_{up} (x/c)	T_{lo} (x/c)	Airfoil Area	Angle of Attack
Initial	31.38	0.2206	0.0070	0.45	0.85	0.08073	2.00^o
Final	101.22	1.1124	0.0110	0.57	0.95	0.08081	4.23^o

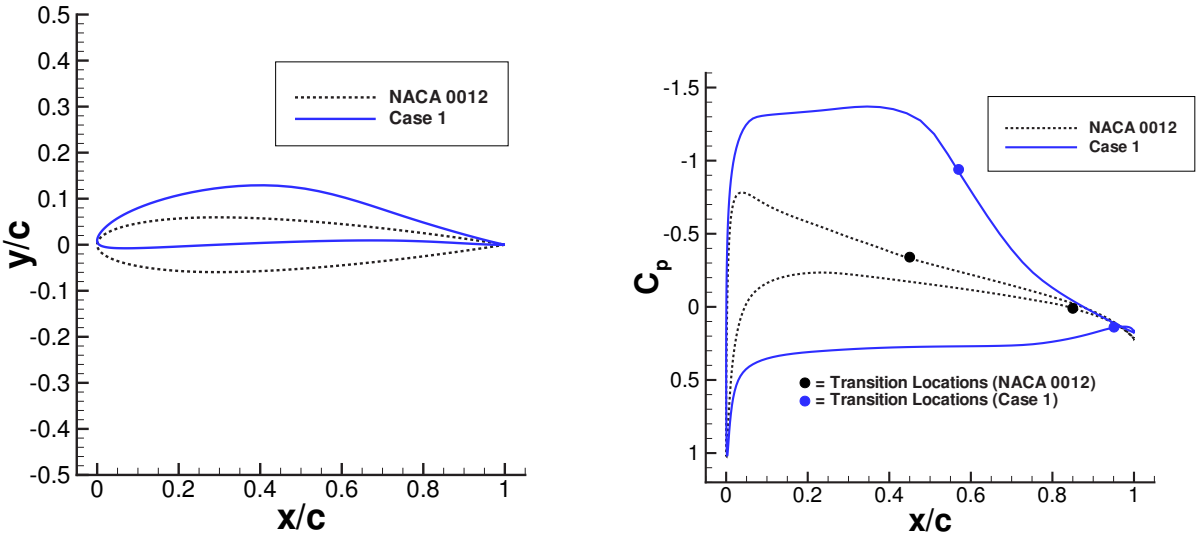

(a) Initial and final airfoils

(b) Initial and final pressure distributions

Figure 5.1: Case 1: Lift-to-drag ratio maximization, M=0.25, Re=1 million

upper surface. The angle of attack is also included as a design variable. The area of the initial airfoil is required to be preserved throughout the optimization process. The area constraint is lifted into the objective function via a penalty method with a weight of 0.1.

Table 5.1 lists the lift-to-drag ratios, transition locations, area values, and angles of attack for both the initial and final airfoils. Figure 5.1 shows the initial and final airfoils and pressure distributions, respectively. **Case 1** shares similar qualities found in high lift-to-drag ratio airfoils at similar operating conditions [63]. The lower surface experiences 95% laminar flow, which is due to the lower surface transition location constraint (Section 4.2.4), while transition occurs at approximately 57% chord on the upper surface. The transition locations on both surfaces moved downstream. The optimizer was able to recognize that increasing the region of laminar flow on the lower surface, through the manipulation of the transition location, allowed for a reduction in drag. Also, the optimizer placed the upper surface transition location to benefit

Table 5.2: Lift-to-drag ratio maximization: Case 2

Case	$\frac{C_L}{C_D}$	C_L	C_D	T_{up} (x/c)	T_{lo} (x/c)	Airfoil Area	Angle of Attack
Initial	28.85	0.2317	0.0080	0.18	0.49	0.08073	2.00^o
Final	101.60	1.1756	0.0116	0.29	0.95	0.08075	5.86^o

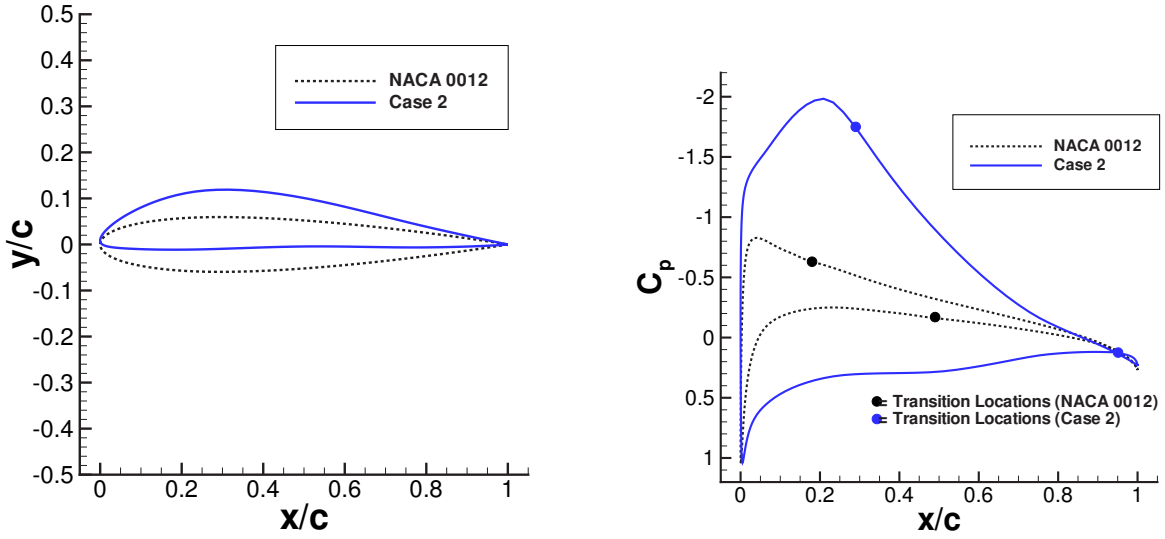

(a) Initial and final airfoils

(b) Initial and final pressure distributions

Figure 5.2: Case 2: Lift-to-drag ratio maximization, M=0.40, Re=10 million

from both the reduction of drag, and the ability to recover the pressure more aggressively.

Case 2: Mach Number = 0.40, Reynolds Number = 10 million

The grid, airfoil parameterization, area constraint, and initial angle of attack is identical to **Case 1** above. The only differences in **Case 2** are the operating conditions. The Mach number is nearly doubled to 0.40, while the Reynolds number is increased tenfold to 10 million.

Table 5.2 lists the lift-to-drag ratios, transition locations, and area values for both the initial and final airfoils. Figure 5.2 shows the initial and final airfoil and pressure distributions, respectively. **Case 2** shows how the Reynolds number affects the optimum, since transition is very sensitive to the Reynolds number. Similar to **Case 1**, the lower surface experiences 95% laminar flow. In order to push the transition location further downstream the favourable pressure gradient on

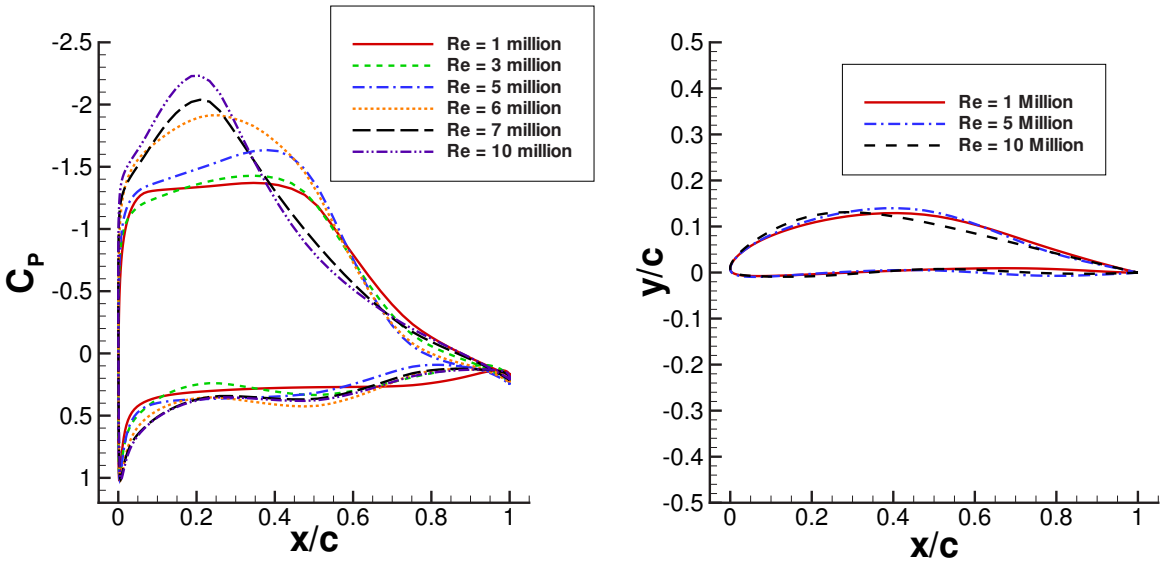

(a) Pressure distributions

(b) Airfoils for Re = 1, 5 and 10 million

Figure 5.3: Case 3: Lift-to-drag ratio maximization, Reynolds number variations

the upper surface is required to be much steeper than the lower Reynolds number case, **Case 1** above. This favorable pressure gradient adds stability to the boundary layer, allowing the transition to be further aft.

Case 3: Mach Number = 0.25, Reynolds Number Variation (1 - 10 million)

In order to examine the effect of the Reynolds number on the optimum designs, a lift-to-drag ratio maximization for Reynolds numbers ranging from 1 to 10 million at a Mach number of 0.25 is studied. The grid, airfoil parameterization, area constraint, and initial angle of attack is identical to **Case 1**.

Figure 5.3(a) shows the final pressure distributions for a range of Reynolds numbers. Figure 5.3(b) shows the final airfoils for a Reynolds numbers of 1, 5 and 10 million. Table 5.3 lists the associated lift-to-drag ratio values, transition locations, airfoil areas, and angles of attack. This experiment demonstrates how the pressure distribution on the upper surface reacts to provide boundary layer stability under different Reynolds numbers. As the Reynolds number increases the pressure distribution on the upper surface gradually becomes steeper to maintain boundary layer stability, as expected.

Table 5.3: Lift-to-drag ratio maximization: Case 3

Reynolds Number ($\times 10^6$)	$\frac{C_L}{C_D}$	T_{up} (x/c)	T_{lo} (x/c)	Angle of Attack
1.0	101.20	0.57	1.00	4.23^o
3.0	118.40	0.53	1.00	4.64^o
5.0	117.32	0.51	0.99	5.35^o
6.0	112.02	0.43	0.95	6.34^o
7.0	102.27	0.31	1.00	6.33^o
10.0	100.20	0.29	1.00	6.80^o

Case 4: M = 0.25, Re = 1 million (Zingg Revisited)

Case 4 uses the grid described for **Case D** in Table 4.1, and is designed at a Mach number of 0.25 and a Reynolds number of 1 million. The initial angle of attack is set to 1 degree. The NACA-64015 airfoil is parameterized using 15 B-spline control points, of which 12 are used as design variables, and the locations are similar to the NACA-0012 airfoil indicated in Figure 2.1. Control points 2-7 are used as design variables on the lower surface, with control points 9-14 used as design variables on the upper surface. The angle of attack is also included as a design variable. The maximum thickness of the NACA-64015 airfoil is required to be maintained throughout the optimization. This is done by using a floating thickness constraint of $(t/c)_{max} = 0.15$ between 10% chord and 90% chord. The thickness constraint is lifted into the objective function with a weighting of 1.0. The NACA-64015 is chosen as the starting airfoil to re-examine the design space that Zingg used to in the design of airfoils with high lift-to-drag ratios [63]. Zingg used NACA thickness forms all with $(t/c)_{max} = 0.15$ to construct velocity distributions with different recovery points. The velocity distributions were used to satisfy a recovery point that resulted in the maximum lift to drag ratio. The purpose of this case study is to re-examine the design space that Zingg explored over 24 years ago.

Table 5.4 lists the lift-to-drag ratios, transition locations, maximum airfoil thickness values, $(t/c)_{max}$, and angles of attack for both the initial, final, and Zingg-1981 airfoils. Figure 5.4 shows the initial and final airfoil and pressure distributions, respectively. **Case 4** shares similar qualities found in high lift-to-drag ratio airfoils at similar operating conditions, such as **Case 1**. For example, the lower surface experiences 95% laminar flow, which is due to the lower surface transition location constraint (Section 4.2.4), while transition occurs at approximately 57% chord on the upper surface. Furthermore, a steep pressure recovery region is present in the turbulent boundary layer on the upper surface.

Table 5.4: Lift-to-drag ratio maximization: Case 4

Case	$\frac{C_L}{C_D}$	C_L	C_D	T_{up} (x/c)	T_{lo} (x/c)	$(t/c)_{max}$	Angle of Attack
Initial	15.09	0.1192	0.0079	0.59	0.63	0.1497	1.00^o
Final	90.42	0.9974	0.0110	0.57	0.95	0.1496	4.28^o
Zingg-1981	83.25	0.8884	0.0107	0.73	0.95	0.1495	1.93^o

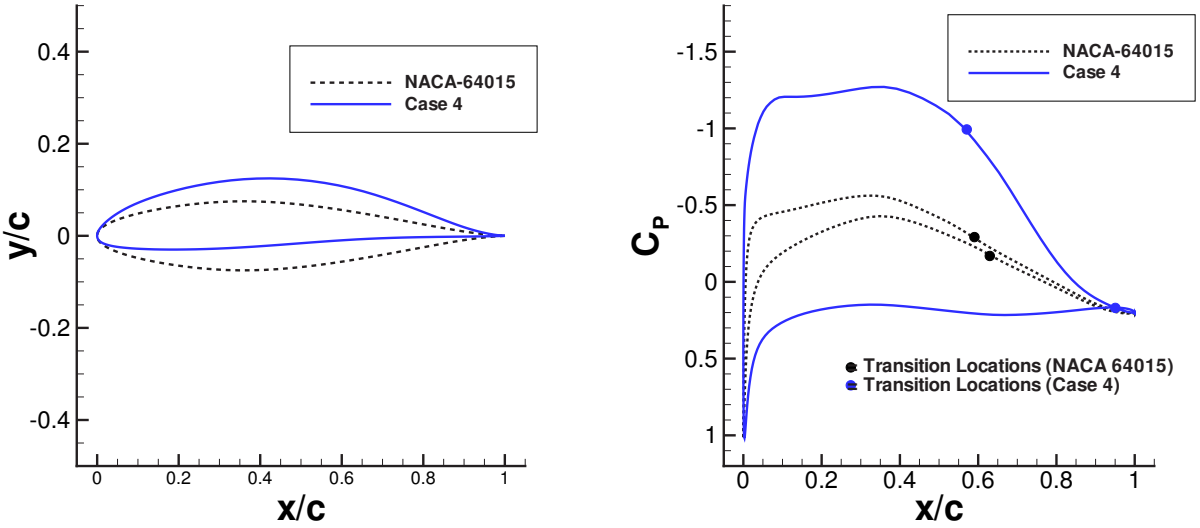

(a) Initial and final airfoils

(b) Initial and final pressure distributions

Figure 5.4: Case 4: Lift-to-drag ratio maximization, M=0.25, Re=1 million

Case D described in Chapter 4 is an example of one of the high lift-to-drag ratio designs Zingg presented. The lift-to-drag ratio of the Zingg-1981 airfoil, at an angle of attack of 1.93, is 83.25. This was found to be the maximum lift-to-drag ratio under these operating conditions. The upper and lower transition locations, which are also listed in Table 4.2, are approximately 73% chord and 95% chord, respectively. **Case 4** was able to produce an airfoil that had an 8% increase in the lift-to-drag ratio with a maximum thickness of approximately 15% chord.

Figure 5.5(a) shows the differences between the coefficient of pressure distributions at the maximum lift-to-drag ratio for **Case 4** and the ZINGG-1981 airfoil. Figure 5.5(b) shows the difference between the airfoil designed in **Case 4** and the ZINGG-1981 airfoil. Designing airfoils within the context of maximizing the lift-to-drag ratio in numerical optimization shares similar challenges to those that Zingg faced in formulating the optimality conditions. For example,

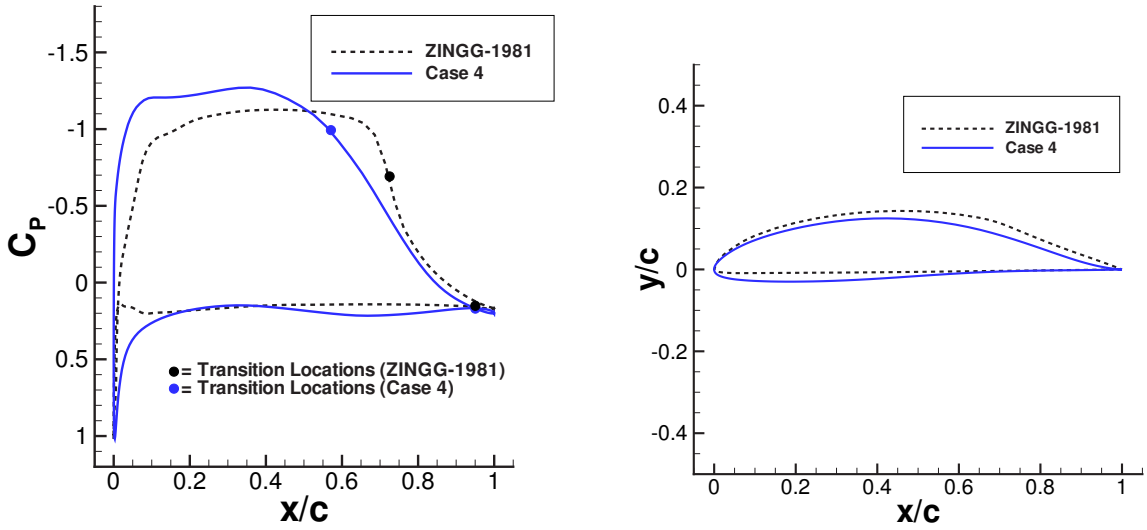

(a) Coefficient of pressure

(b) Airfoils

Figure 5.5: Case 4 and the ZINGG-1981 airfoil

the location of the upper surface transition location is paramount to insure pressure recovery without separation. This was automatically detected in the numerical optimization routine since the objective function is penalized if separation occurs via an increase in drag. Furthermore the optimizer forces the transition location further downstream to benefit from the reduction in drag. This causes the upper surface pressure distribution to be extremely flat. The ZINGG-1981 airfoil demonstrated a longer run of laminar flow on the upper surface and a steeper pressure recovery.

5.3 Endurance Factor

The maximization of the endurance factor, Equation 2.6, of a fully turbulent design and a laminar-turbulent design is presented in this section. The two designs are quantitatively compared, and the trade-offs between the two designs are investigated through the use of a Pareto front using the weighted-sum approach.

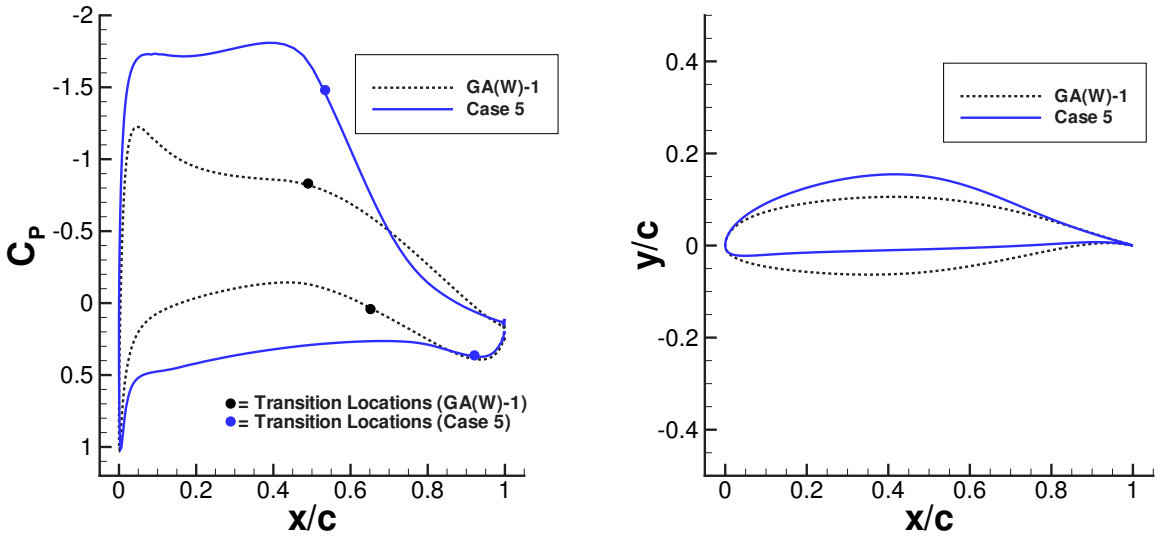

(a) Initial and final pressure distributions

(b) Initial and final airfoils

Figure 5.6: Case 5: Endurance factor maximization (laminar-turbulent), M=0.20, Re=2 million

Case 5: Mach Number = 0.20, Reynolds Number = 2 million

Case 5 uses the grid described for **Case A** in Table 4.1, and is designed assuming laminar-turbulent conditions at a Mach number of 0.20 and a Reynolds number of 1 million. The initial angle of attack is set to 2.44 degrees. The initial angle of attack is chosen to be at the maximum endurance factor for the GA(W)-1 airfoil under these conditions. The airfoil is parameterized using 15 B-spline control points, of which 6 are used as design variables, and the locations are similar to those indicated in Figure 2.1. Control points 4-6 are used as design variables on the lower surface, with control points 10-12 used as design variables on the upper surface. The angle of attack is also included as a design variable. Table 5.5 shows the thickness constraints used to avoid invalid shapes during the optimization iterations, and the final thickness distribution. The thickness constraints are lifted into the objective function via a penalty method with a weight of 1.0. Table 5.6 lists the endurance factor, force coefficients, transition locations, and angle of attack for both the initial and final airfoils. The results from this experiment demonstrate similar qualities that were present in **Case 1**, the development of a laminar roof-top and the lower surface experiencing a long run of laminar flow. The thickness constraint at 35% chord was marginally violated in the final design. Figure 5.6(a) compares the initial and final coefficient of pressure distributions. Figure 5.6(b) compares the initial and final airfoils. The endurance factor improved from approximately 62 to 115.5, an increase of

Table 5.5: Case 5: Thickness constraints

x/c	0.15	0.35	0.60	0.92	0.99
t/c (constraint)	0.0100	0.1640	0.0700	0.0100	0.0010
t/c (final)	0.1293	0.1637	0.1332	0.0136	0.0012

Table 5.6: Endurance factor maximization: Case 5

Case	$\frac{C_L^{3/2}}{C_D}$	C_L	C_D	T_{up} (x/c)	T_{lo} (x/c)	Angle of Attack
Initial	61.99	0.7264	0.0099	0.49	0.65	2.44^o
Final	115.50	1.4598	0.0153	0.54	0.92	5.97^o

Table 5.7: Case 6: Thickness constraints

x/c	0.15	0.35	0.60	0.92	0.99
t/c (constraint)	0.0100	0.1640	0.0700	0.0100	0.0010
t/c (final)	0.1621	0.1634	0.1061	0.0099	0.0011

87%.

Case 6: Mach Number = 0.20, Reynolds Number = 2 million

Case 6 is set-up identically to **Case 5**, except that the transition locations are at the leading edge, i.e. fully turbulent conditions. The initial angle of attack is set to 7.53^o, which results in the maximum endurance factor for the GA(W)-1 under fully turbulent conditions. Table 5.7 gives the thickness constraints used to avoid invalid shapes during the optimization iterations, which are the same as **Case 5**, and the final thickness distribution. Table 5.8 lists the endurance factors, force coefficients, and angles of attack for both the initial and final airfoils. (The results from this experiment are similar to those presented in **Case 7DV** of Hua et al. [20]). The thickness constraints at 35% chord and 92% chord are marginally violated in the final design. Figure 5.7(a) compares the initial and final coefficient of pressure distributions. Figure 5.7(b) compares the initial and final airfoils.

Table 5.8: Endurance factor maximization: Case 6

Case	$\frac{C_L^{3/2}}{C_D}$	C_L	C_D	Angle of Attack
Initial	49.24	1.1654	0.0256	7.53^o
Final	59.83	1.3793	0.0271	7.24^o

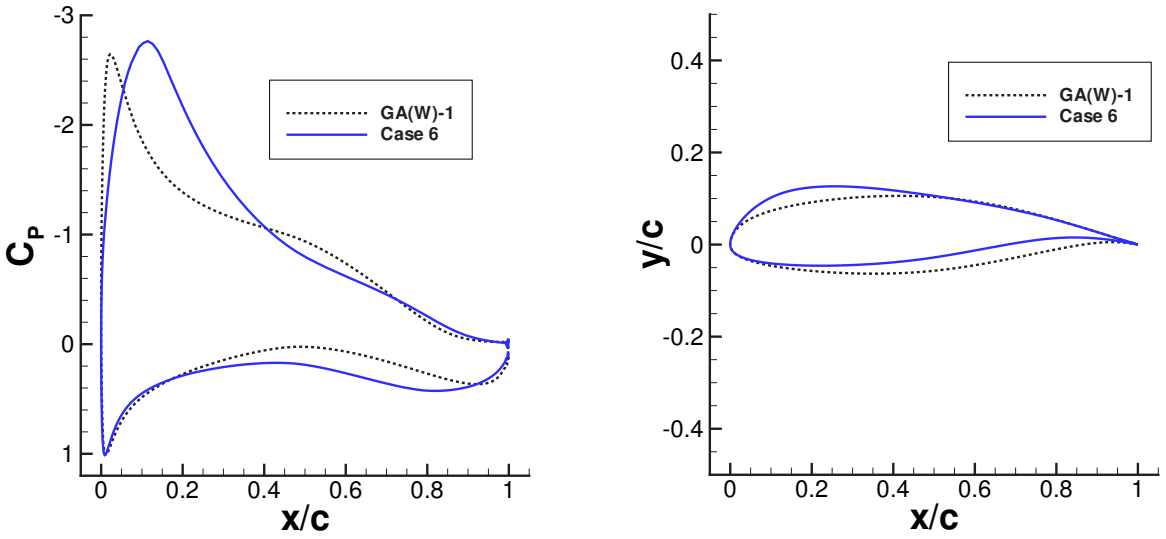

(a) Initial and final pressure distributions

(b) Initial and final airfoils

Figure 5.7: Case 6: Endurance factor maximization (fully turbulent), M=0.20, Re=2 million

Comparison between Cases 5 and 6

Although **Case 5** is able to produce an airfoil that has an endurance factor nearly twice that of the **Case 6**, it is an unfair comparison. To compare the two designs quantitatively, it is necessary find the best off-design performance of both airfoils with respect to transition. The best off-design performance for **Case 5** is found by determining the angle of attack that produces the maximum endurance factor when transition occurs at the leading edge on both surfaces. The best off-design performance for **Case 6** is found by determining the angle of attack that produces the maximum endurance factor when transition occurs naturally. Table 5.9 lists the endurance factor, force coefficients, transition locations, and angles of attack for **Cases 5** and **6** for off-design conditions. Figure 5.8 compares the on-design and off-design coefficient of pressure distributions for Cases 5 and 6, respectively. A couple of interesting points can be made from

Table 5.9: Endurance factor maximization comparison: Case 5 versus Case 6

Case	$\frac{C_L^{3/2}}{C_D}$	C_L	C_D	T_{up} (x/c)	T_{lo} (x/c)	Angle of Attack
Case 5[a]	41.61	0.9887	0.0236	-	-	2.70^o
Case 6[b]	85.69	1.5571	0.0227	0.19	0.66	8.27^o

[a] fully turbulent conditions
[b] laminar-turbulent conditions

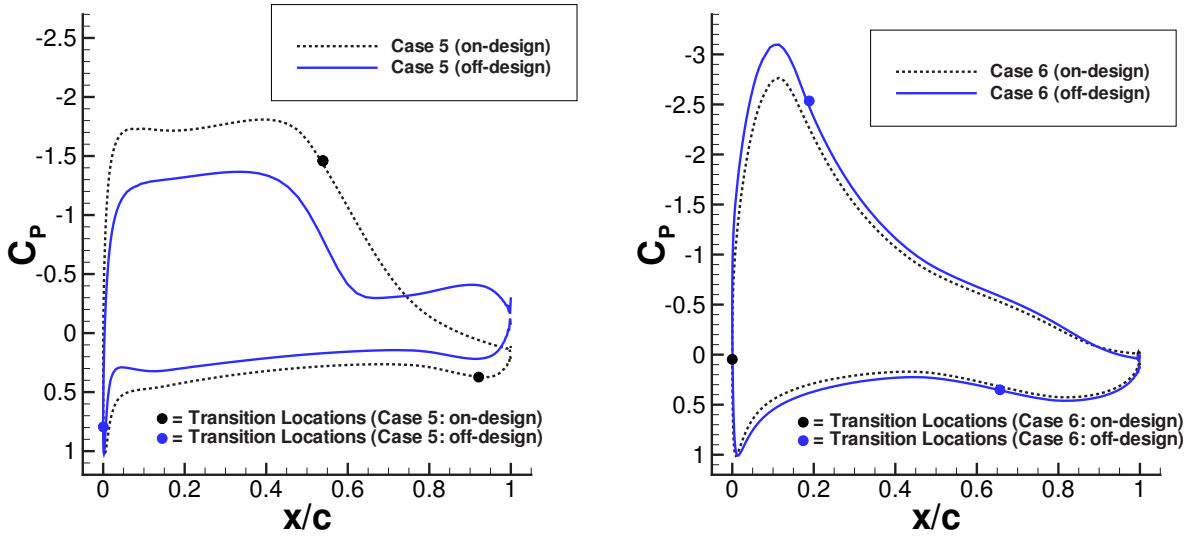

(a) Initial and final pressure distributions

(b) Initial and final pressure distributions

Figure 5.8: Off-design performance of Cases 5 and 6

the off-design comparison of both airfoils. First, **Case 5** under laminar-turbulent conditions produces a higher endurance factor than **Case 6** analyzed under the same conditions. Second, **Case 5** under fully turbulent conditions has very poor performance. Obviously this is not a desirable aerodynamic property. It is desirable to design an airfoil that exploits the advantages of having maximum laminar flow under ideal conditions but also performs well when transition occurs further forward than expected. These trade-offs can be assembled into a family of non-inferior designs, or a Pareto front.

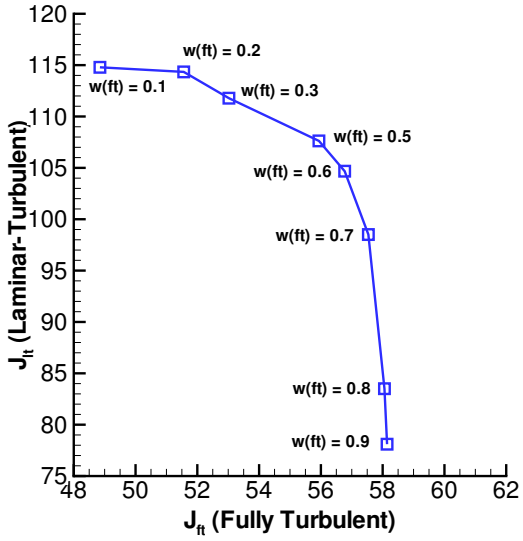

Figure 5.9: Pareto front: laminar-turbulent versus fully turbulent endurance factor maximization

Endurance Factor Pareto Front

In order to form a Pareto front, the weighted-sum method is used:

$$\mathcal{J} = \omega_{ft}\mathcal{J}_{ft} + (1 - \omega_{ft})\,\mathcal{J}_{lt} \tag{5.1}$$

where $\mathcal{J}_{ft}$ and $\mathcal{J}_{lt}$ are the objective function values of Equation 2.6 under fully turbulent and laminar-turbulent conditions, respectively. Thickness constraints are used to avoid invalid shapes during the optimization iterations. The thickness constraints are lifted into the objective function via a penalty method with a weight of 1.0 and are listed in the t/c (constraint) row in Table 5.5.

An important point to make is that at each Pareto front location a two-point design problem is solved. The two points are a laminar-turbulent analysis and a fully turbulent analysis. The initial conditions are identical to **Cases 5** and **6**. The computed Pareto front is shown in Figure 5.9, where the trade-offs associated with favouring one operating condition over the other are clearly captured. Table 5.10 lists the coefficients of lift and drag for the selected solutions contained in the Pareto front. Figure 5.10 shows selected Pareto front airfoils and the laminar-turbulent pressure distributions, respectively. Interesting trade-offs between fully turbulent and laminar-turbulent designs can be understood through the results of this design case. For example, if one is aggressive and uses ω_{ft}=0.1, then one pays a huge price if transition

Table 5.10: Aerodynamic coefficients and endurance factor values for selected Pareto-optimal solutions

	Fully Turbulent		Laminar-Turbulent		Fully Turbulent	Laminar-Turbulent
ω_{ft}	C_L	C_D	C_L	C_D	$\frac{C_L^{3/2}}{C_D}$	$\frac{C_L^{3/2}}{C_D}$
0.1	1.088	0.0233	1.384	0.0142	48.84	114.7
0.2	1.127	0.0232	1.383	0.0142	51.55	114.2
0.3	1.126	0.0225	1.285	0.0130	53.02	111.7
0.5	1.213	0.0239	1.292	0.0137	55.90	107.5
0.6	1.259	0.0249	1.212	0.0128	56.72	104.4
0.7	1.235	0.0239	1.105	0.0118	57.48	98.34
0.8	1.270	0.0247	1.134	0.0145	57.96	83.31
0.9	1.308	0.0257	1.036	0.0135	58.01	77.86

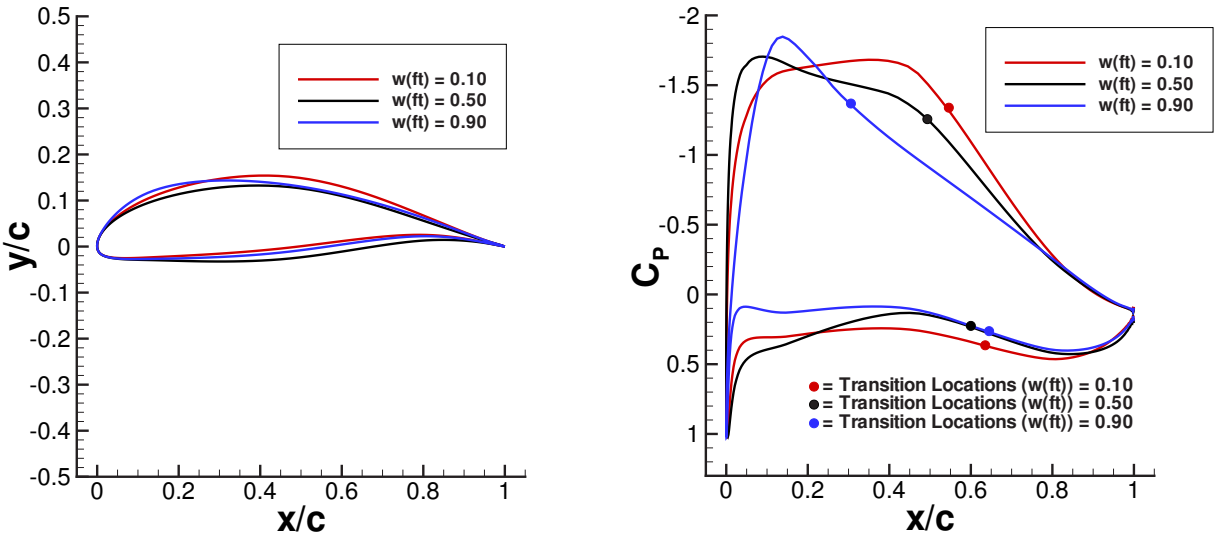

(a) Selected Pareto front airfoils

(b) Selected Pareto front laminar-turbulent pressure distributions

Figure 5.10: Cases 5 and 6: M=0.20, Re=2 million

occurs at the leading edge; the endurance factor drops from approximately 115 to 49. If one is conservative and uses ω_{ft}=0.9, then the gain when laminar flow is achieved is minimal. With intermediate values of ω_{ft}, for example $0.3 \leq w_{ft} \leq 0.7$, the off-design performance improves without too large a penalty on-design. For example, with ω_{ft}=0.5, the fully turbulent endurance factor is approximately 56 while the on-design laminar-turbulent endurance factor is approximately 107.

Table 5.11: Lift-constrained drag minimization: Case 7

Case	C_L	C_D	T_{up} (x/c)	T_{lo} (x/c)	Airfoil Area	Angle of Attack
Initial	0.4932	0.0088	0.11	0.52	0.0777	2.00^o
Final	0.5870	0.0056	0.54	0.78	0.0776	1.67^o

5.4 Lift-Constrained Drag Minimization

Lift-constrained drag minimization, Equation 2.4, is presented in this section with achievable lift and unachievable drag targets.

Case 7: Mach Number = 0.40, Reynolds Number = 10 million

Case 7 uses the RAE-2822 airfoil as the initial shape with the grid parameters described for **Case D** in Table 4.1. The design is performed at a Mach number of 0.40 and a Reynolds number of 10 million. The initial angle of attack is 2 degrees. The airfoil is parameterized using 15 B-spline control points, of which 12 are used as design variables, and the locations are similar to those indicated in Figure 2.1. Control points 2-7 are used as design variables on the lower surface, with control points 9-14 used as design variables on the upper surface. The angle of attack is also included as a design variable. The area of the initial airfoil is required to be preserved throughout the optimization process. The target lift coefficient is 0.5968, which is approximately a 21% increase in lift. The target drag coefficient is 0.0054, which is approximately a 39% reduction in drag. The weights on the coefficient of lift, drag, and the area constraint are 2.0, 1.0 and 1.0, respectively. Table 5.11 lists the initial and final coefficients of lift, drag, transition locations, airfoil areas, and angles of attack. Figure 5.11 shows the initial and final pressure coefficient distributions and airfoils, respectively. The upper surface experiences a favorable pressure gradient to approximately 40% chord. This improves the boundary layer stability, allowing transition to occur further aft. The minimum pressure on the lower surface was also pushed further downstream, allowing a longer run of laminar flow. The constraint on preserving the initial RAE 2822 airfoil area is active in the final design. The final design is 1.64% below the target coefficent of lift and 3.57% above the target drag coefficent.

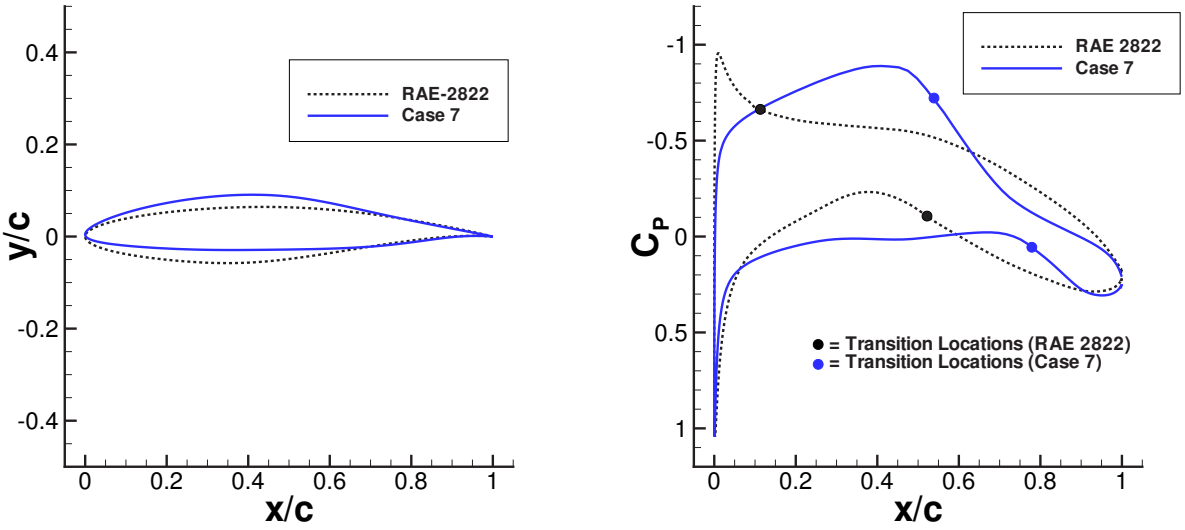

(a) Initial and final airfoils

(b) Initial and final pressure distributions

Figure 5.11: Case 7: Lift-constrained drag minimization, M=0.40, Re=10 million

5.5 Lift Maximization

This section discuss three lift maximization cases:

- lift maximization allowing boundary-layer separation to occur
- lift maximization with a constraint on the amount of boundary-layer separation,
- lift maximization with a constraint on boundary-layer separation and the pitching moment.

A subtle point that should be reiterated here is that every objective function evaluation and objective function gradient evaluation is started from free-stream conditions. The dangers of warm-starting the solution under laminar-turbulent conditions are discussed in Section 4.2.3. This fact will limit the maximum lift possible due to flow solver problems.

Case 8: Lift Maximization

In order to maximize lift, we set the weight on the drag target, ω_D in Equation 2.4, to zero and the target lift is required to be unobtainable. This is similar to other maximization of lift cases

Table 5.12: Case 8: Thickness constraints

x/c	0.06	0.25	0.60	0.80	0.95
t/c (constraint)	0.0800	0.1000	0.0550	0.0200	0.0100
t/c (final)	0.1521	0.0996	0.0651	0.0265	0.0099

Table 5.13: Case 8: Maximization of lift

Case	C_L	C_D	T_{up} (x/c)	T_{lo} (x/c)	Angle of Attack
Initial	0.2188	0.0066	0.37	0.75	2.00^o
Final	2.0937	0.0277	0.36	0.95	11.70^o

studied by Nemec and Zingg [38]. **Case 8** uses the grid described for **Case B** in Table 4.1, and is designed at a Mach number of 0.25 and a Reynolds number of 2 million. The initial angle of attack is set to 2 degrees. The airfoil is parameterized using 15 B-spline control points, of which 12 are used as design variables; the locations are indicated in Figure 2.1. Control points 2-7 are used as design variables on the lower surface, with control points 9-14 used as design variables on the upper surface. The angle of attack is also included as a design variable. Table 5.12 shows the thickness constraints used to avoid invalid shapes during the optimization iterations. The thickness constraints are lifted into the objective function with a weight of 0.05. The initial angle of attack is 2 degrees. The target lift coefficient is 2.10. Table 5.13 lists the initial and final coefficients of lift, drag, transition locations, and angles of attack. Figure 5.12 shows the initial and final coefficient of pressure distributions and airfoils, respectively. **Case 8** experienced maximum lift with boundary-layer separation occurring at 86% chord on the upper surface while the lower surface remained fully attached with the transition location being constrained to 95% chord. The thickness constraints at 25% chord and 95% chord were mildly violated in the final design. As required by the objective function, the operating conditions for **Case 8** occurred just before stall conditions. This can be demonstrated by analyzing the coefficient of lift, drag, and pitching moment of the designed airfoil in **Case 8** by varying the angle of attack, and is graphically shown in Figure 5.13. The boundary layer separates at an angle of attack of 9^o with $C_L = 1.85$, after which separation point moves forward. A challenge with designing airfoils at maximum lift within the context of numerical optimization is insuring reliable gradients and objective function evaluations. Since the designs are near stall conditions, flow solver convergence problems are common. Furthermore, the probability of having poorly converged solutions increases due to the fact that warm starting the flow solution is prohibited. This not only causes problems with gradient accuracy but also with the objective function

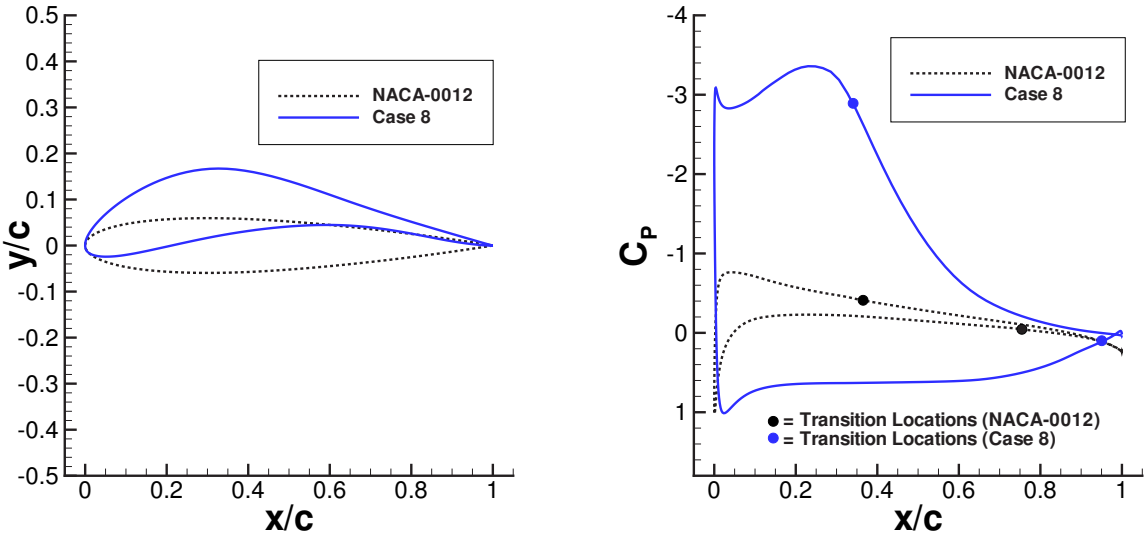

(a) Initial and final airfoils

(b) Initial and final pressure distributions

Figure 5.12: Case 8: Maximization of lift, M=0.25, Re=2 Million

evaluation.

Case 9: Lift Maximization with Separation Constraint

The design of **Case 9** is identical to **Case 8** except that a constraint on the amount of boundary layer separation is introduced into Equation 2.4. The resulting objective function is as follows:

$$\begin{aligned} \mathcal{J} &= \omega_L \left(1 - \frac{C_L}{C_L^*}\right)^2 \\ &+ \frac{\omega_{C_f}}{N} \left(\sum_{i=1}^{N} \left(1 - \frac{C_f(x_i)}{C_f^*(x_i)}\right)^2\right) \quad \text{if} \quad |\, C_f(x_i) \,| < C_f^*(x_i) \quad \text{and} \quad x_{start} \leq x_i \leq x_{end} \\ &+ T.C. \end{aligned} \tag{5.2}$$

where C_L^* is the target lift, $C_f^*(x_i)$ is the skin friction coefficients at airfoil location x_i, ω_L and ω_{C_f} are user defined constants, and T.C. is the thickness constraints. The constants x_{start} and x_{end} are the user defined bounds over which the coefficient of friction constraint is evaluated on the airfoil surface. The weight on the coefficient of friction term, ω_{C_f}, is normalized with respect to the number of violated nodes, N. It is important to note that summation operator in Equation 5.2 only sums those nodes that violate the two conditions: the boundary limits (x_{start} and x_{end}), and the coefficient of friction target ($C_f^*(x_i)$). The thickness constraints, identical

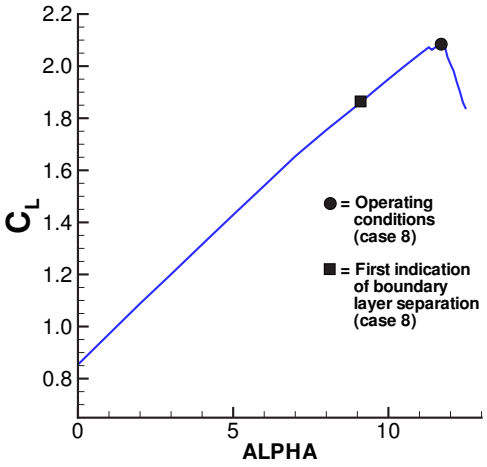

(a) Coefficient of lift (C_L) variation

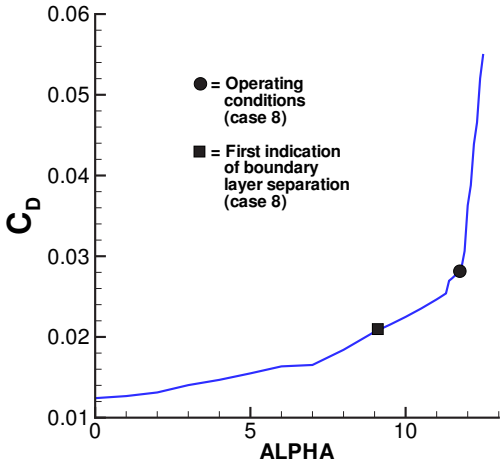

(b) Coefficient of drag (C_D) variation

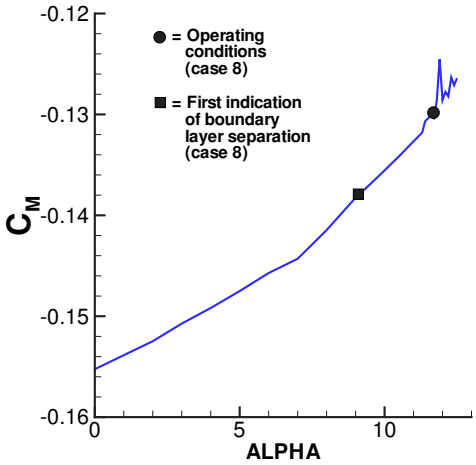

(c) Coefficient of pitching moment (C_M) variation

Figure 5.13: Case 8: C_L, C_D and C_M as function of angle of attack, M=0.25, Re=2 Million

to **Case 8**, have a weight of 0.05. The weights on the coefficient of lift and friction terms are 2.0 and 1.0, respectively. The initial angle of attack is set to 2 degrees. The target coefficients of lift and friction are 1.72 and 0.001, respectively. Table 5.14 shows the thickness constraints.

Table 5.15 lists the initial and final coefficients of lift, transition locations, and angles of attack. Figure 5.14 shows the initial and final pressure coefficient distributions and airfoils. Figure 5.15

Table 5.14: Case 9: Thickness constraints

x/c	0.06	0.25	0.60	0.80	0.95
t/c (constraint)	0.0800	0.1000	0.0550	0.0200	0.0100
t/c (final)	0.0785	0.1309	0.0558	0.0171	0.0042

Table 5.15: Case 9: Lift maximization with separation constraint

Case	C_L	C_D	T_{up} (x/c)	T_{lo} (x/c)	Angle of Attack
Initial	0.2188	0.0066	0.37	0.75	2.00^o
Final	1.6937	0.0181	0.38	0.95	8.56^o

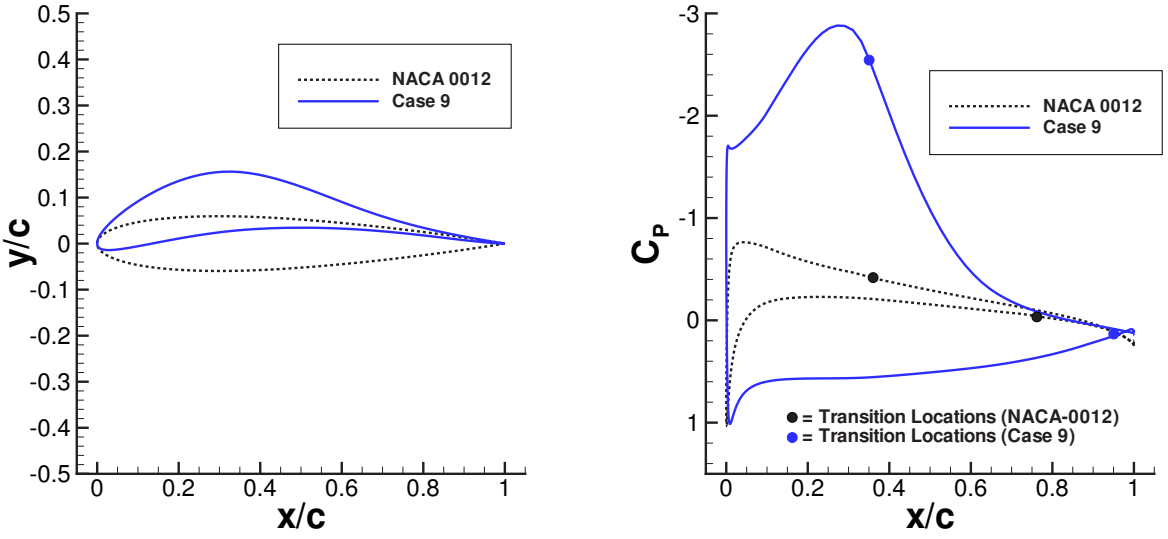

(a) Initial and final airfoils

(b) Initial and final pressure distributions

Figure 5.14: Case 9: Lift maximization with separation constraint, M=0.25, Re=2 Million

shows the final coefficient of friction distribution on the airfoil surface. The coefficient of friction on the lower surface of the airfoil is plotted negative for clarity. The coefficient of friction constraint introduced into the objective function increased the sensitivity of the transition location on the upper surface. This encouraged the optimizer to design an airfoil with an upper surface transition location that allows the pressure recovery in the turbulent boundary to remain fully attached. One observation is that additional lift could be realized by decreasing the coefficient of pressure distribution on the upper surface upstream of the

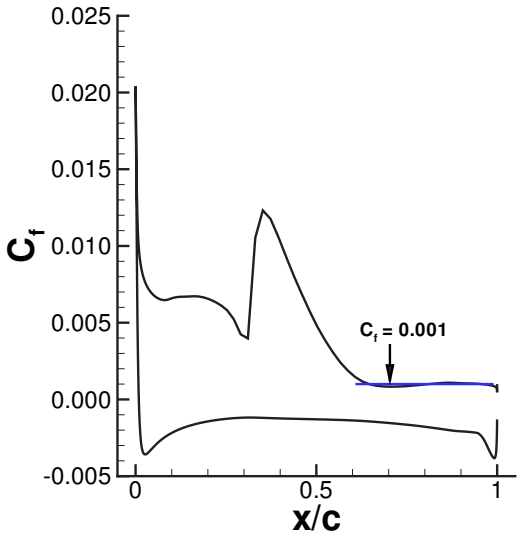

Figure 5.15: Case 9: Coefficient of friction, M=0.25, Re=2 Million

transition location. This action would improve lift but at the sacrifice of a reduced pressure gradient causing instabilities in the boundary layer to amplify at a faster rate. This would eventually lead to the breakdown of laminar flow leading to turbulent transition earlier. The upstream movement of the transition location would cause the turbulent boundary layer in the pressure recovery region to violate the coefficient of friction constraint.

As shown in Figure 5.16, the maximum lift of the design occurred at an angle of attack of 11^o with a lift coefficient of 1.95. Flow separation exists at this angle of attack.

Case 10: Lift Maximization with Pitching Moment and Separation Constraint (Liebeck Revisited)

A famous example of the maximization lift is the popular Liebeck class of airfoils [27]. Liebeck posed the problem as follows:

1. the boundary layer does not separate;
2. the corresponding airfoil shape is practical and realistic; and
3. maximum possible C_L is obtained.

The presented algorithm allows us to revisit the design problem that Liebeck posed over 30 years ago. In order to meet the requirement that no separation is allowed to occur we set

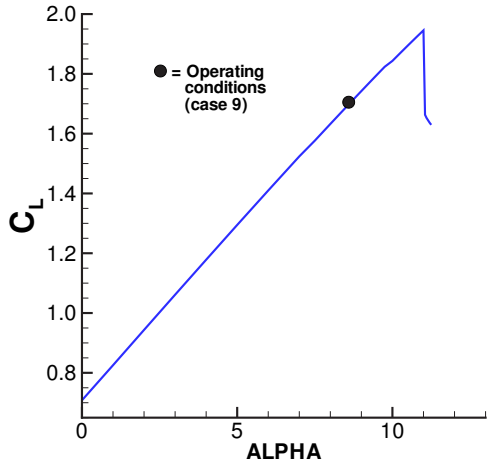

(a) Coefficient of lift (C_L) variation

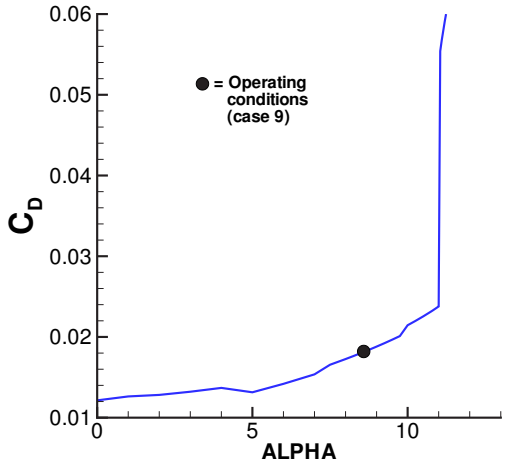

(b) Coefficient of drag (C_D) variation

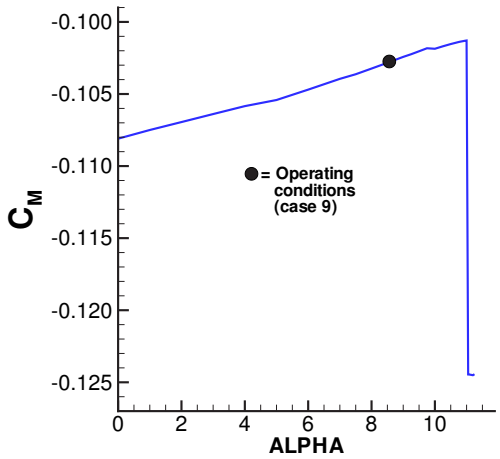

(c) Coefficient of pitching moment (C_M) variation

Figure 5.16: Case 9: C_L, C_D and C_M as function of angle of attack, M=0.25, Re=2 Million

a constraint on the coefficient of friction. Imposing thickness constraints on the airfoil shape enforces the second condition that Liebeck posed. Before the composite objective function used in this case study of maximization of lift is introduced, it is also important to mention two additional constraints that Liebeck imposed on the lower surface velocity distribution:

1. the velocity remains as low as possible in the interest of obtaining the maximum lift

Table 5.16: Case 10: Thickness constraints

x/c	0.06	0.25	0.60	0.80	0.95
t/c (constraint)	0.0800	0.1000	0.0550	0.0200	0.0100
t/c (final)	0.0781	0.1311	0.0610	0.0245	0.0082

possible

2. the flow continuously accelerates from the leading edge stagnation point to the trailing edge velocity in the interest of minimizing drag.

These constraints can be introduced into the objective function by providing a constraint on the pitching moment. The resulting composite objective function is as follows:

$$\begin{aligned} \mathcal{J} &= \omega_L \left(1 - \frac{C_L}{C_L^*}\right)^2 \\ &+ \omega_M \left(1 - \frac{C_M}{C_M^*}\right)^2 \\ &+ \frac{\omega_{C_f}}{N} \left(\sum_{i=1}^{N} \left(1 - \frac{C_f(x_i)}{C_f^*(x_i)}\right)^2\right) \quad \text{if} \quad \mid C_f(x_i) \mid < C_f^*(x_i) \quad \text{and} \quad x_{start} \leq x_i \leq x_{end} \\ &+ T.C. \end{aligned} \tag{5.3}$$

Equation 5.3 is similar to Equation 5.2 except with the introduction of the pitching moment constraint. The pitching moment constraint is evaluated in a similar manner to the lift-constraint, where C_M^* represents the target moment coefficient and ω_M is a user defined constant.

As in **Case 8**, the thickness constraints have a weight of 0.05. The weights on the coefficient of lift, moment, and friction are 2.0, 1.0 and 1.0, respectively. **Case 10** was optimized at a Mach number of 0.25 and a Reynolds number of 2 million. The initial angle of attack is 2 degrees. The target coefficients of lift, moment and friction are 1.60, -0.032 and 0.001, respectively. Table 5.16 shows the thickness constraints used to avoid invalid shapes during the optimization iterations.

Table 5.17 lists the initial and final coefficients of lift, moment, transition locations, and angles of attack. Figure 5.17 shows the initial and final coefficient of pressure distributions and airfoils, respectively. Figure 5.18 shows the final coefficient of friction distribution on the airfoil surface. The coefficient of friction constraint and maximum lift target are two competing objectives. This can be demonstrated by analyzing the coefficient of lift, drag, and pitching moment of the designed airfoil in **Case 10** by varying the angle of attack, and is shown graphically in Figure 5.19. The optimal operating conditions, as listed in Table 5.17, are indicated on Figure 5.19. The actual maximum lift of the design occurs at an angle of attack of 12.1^o with

Table 5.17: Case 10: Lift maximization with pitching moment and separation constraint

Case	C_L	C_M	T_{up} (x/c)	T_{lo} (x/c)	Angle of Attack
Initial	0.2188	0.0028	0.37	0.75	2.00^o
Final	1.5812	-0.0324	0.33	0.95	10.06^o

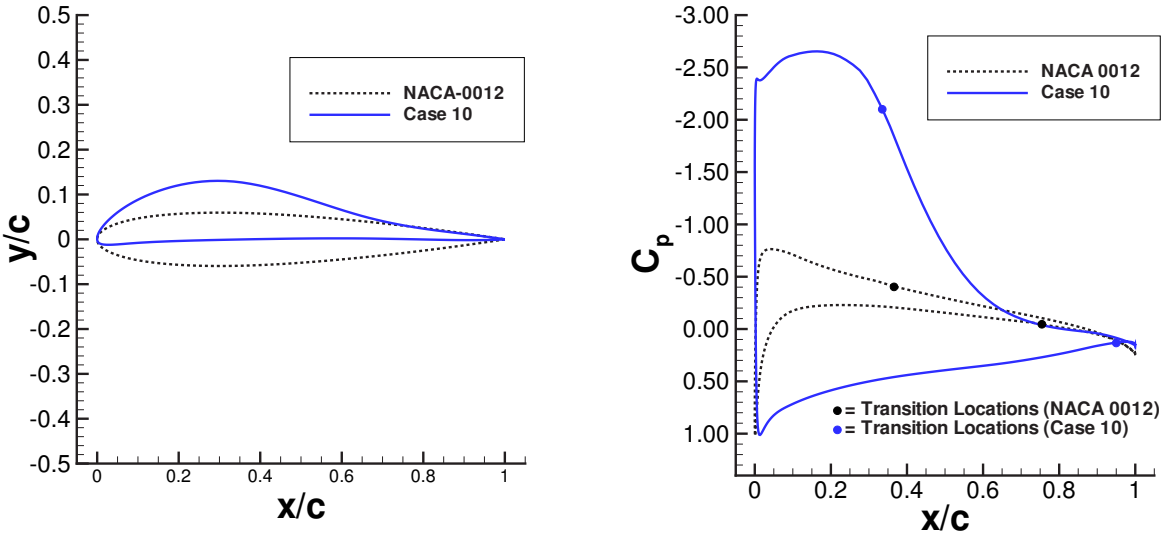

(a) Initial and final airfoils

(b) Initial and final pressure distributions

Figure 5.17: Case 10: Lift maximization with pitching moment and separation constraint, M=0.25, Re=2 Million

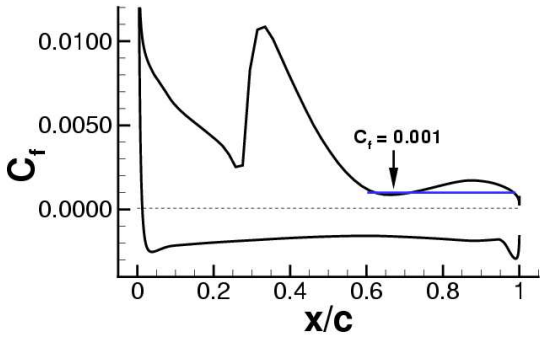

Figure 5.18: Case 10: Coefficient of friction, M=0.25, Re=2 Million

a coefficient of lift of 1.77.

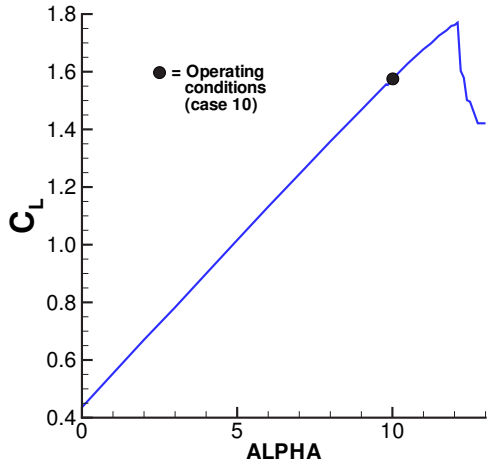

(a) Coefficient of lift (C_L) variation

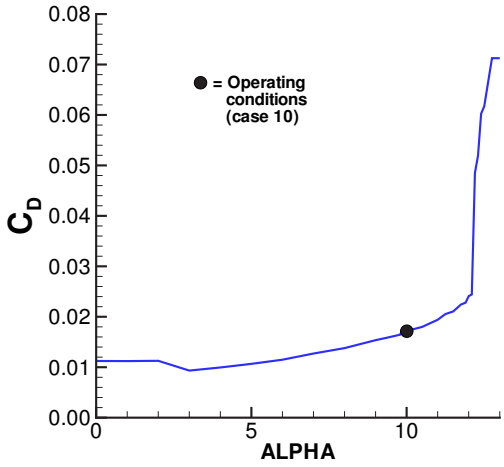

(b) Coefficient of drag (C_D) variation

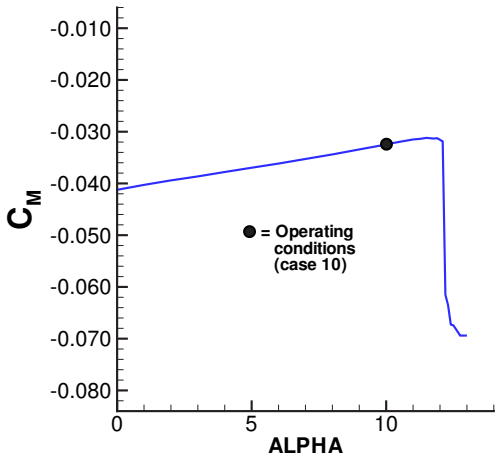

(c) Coefficient of pitching moment (C_M) variation

Figure 5.19: Case 10: C_L, C_D and C_M as function of angle of attack, M=0.25, Re=2 Million

Case 10 demonstrates that, given the objective function in Equation 5.3, the optimizer is able to produce airfoils that share similar qualities to those of Liebeck. For example, the airfoil produced from the optimization experiences a laminar "roof-top", while the flow over the entire lower surface is accelerating and laminar. In addition, concave pressure recovery is shown in Figure 5.17(b). An interesting exercise is to compare the variation of the coefficients of

lift, drag, and pitching moment between the LNV109A Liebeck airfoil[1] (**Case B** described in Chapter 4) and **Case 10**. Furthermore, the coefficient of pressure distributions are compared at a lift coefficient of 1.5812. The results from these comparisons are shown in Figure 5.20. The resulting airfoil from **Case 10** is also compared to the LNV109A airfoil in Figure 5.21.

The variations of C_L and C_D for **Case 10** are remarkably close to those of the LNV109A airfoil. The largest differences between the two airfoils are in the coefficient of moment variation, and the drag coefficient near an angle of attack of zero. **Case 10** was designed to minimize the pitching moment at the operating conditions, which is not completely necessary to achieve a lower surface that experiences accelerated flow. Even greater similarity between the two airfoil shapes may be realized if the pitching moment is increased to that of the LNV109A. Most importantly, the optimizer was able to design an airfoil that shared similar aerodynamic properties of a Liebeck designed airfoil: a laminar "roof-top", an accelerating laminar lower surface, and a concave pressure recovery in the turbulent region on the upper surface.

[1]Operating at a Mach number of 0.25 and a Reynolds number of 2 million

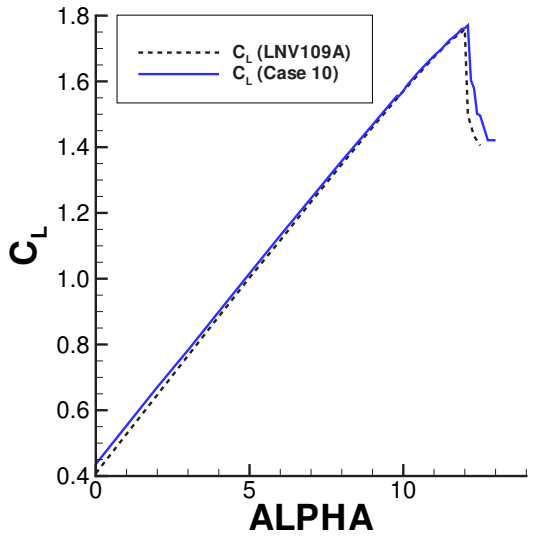

(a) C_L variation

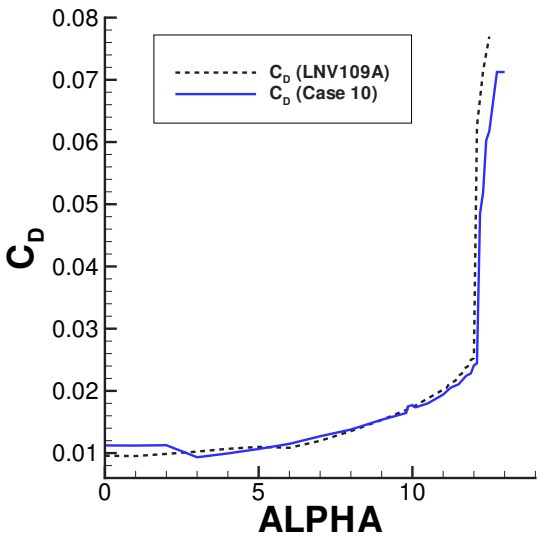

(b) C_D variation

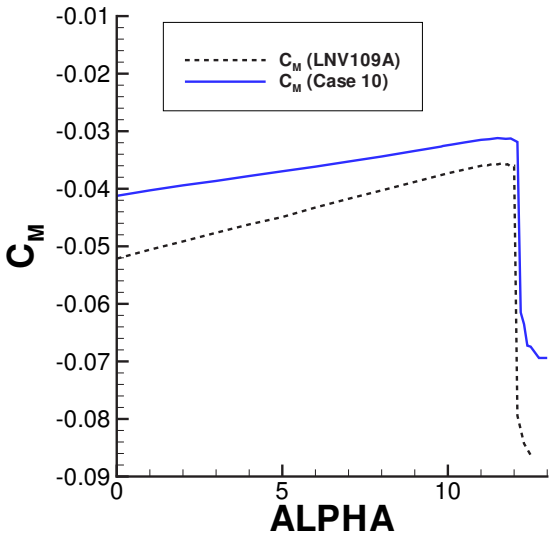

(c) C_M variation

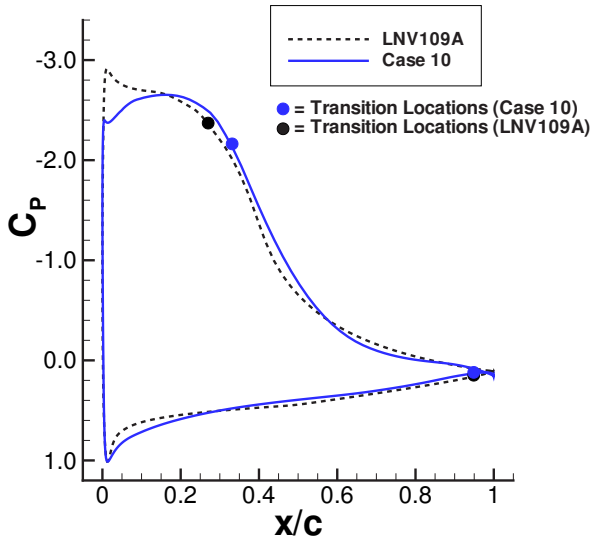

(d) Pressure distributions ($C_L = 1.5812$)

Figure 5.20: Aerodynamic performance comparison between Case 10 and the LNV109A airfoil, M=0.25, Re=2 Million

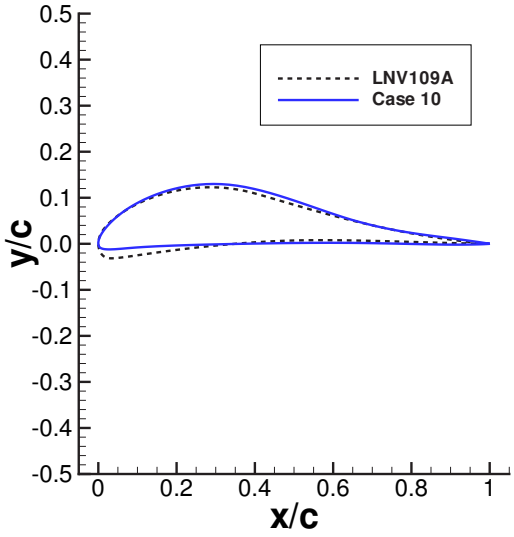

Figure 5.21: Case 10 and the LNV109A airfoil

Chapter 6

Conclusions and Recommendations

A two-dimensional single-element shape optimization routine that manipulates the boundary-layer transition location through shape changes has been developed. Modifications to the existing fully-turbulent shape optimization routine developed by Nemec and Zingg consisted of: implementation of the trip terms in the Spalart-Allmaras turbulence model within the Newton-Krylov framework, a routine to obtain boundary-layer transition locations, and modifications to the discrete-adjoint gradient calculation. The trip terms within the Spalart-Allmaras turbulence model were linearized and introduced into the approximate flow Jacobian used to precondition the governing equations in the Newton-Krylov flow solver. The transpose of the complete flow Jacobian was also used to solve for the adjoint variables used in the discrete-adjoint gradient calculation. The Euler/boundary-layer solver MSES was used to obtain the location of boundary-layer transition. MSES was also used to obtain the sensitivity of the transition locations due to shape changes. This sensitivity was combined, via the chain rule, with the sensitivity of the objective function due to perturbations in the transition locations. The combination of these two sensitivities into the objective function gradient allowed the optimizer to successfully manipulate the transition locations through airfoil shape changes.

The presented algorithm was evaluated based on the ability of the optimizer to produce airfoils that clearly exploited the boundary-layer transition location. The new routine re-examined previously studied optimization cases of Nemec et al. [36], Hua et al. [20], Zingg [63], and Liebeck [27]. The following conclusions can be drawn from the evaluation of the presented algorithm:

1. In order to successfully manipulate the transition locations, based on the RANS equations coupled with a turbulence model, the objective function gradient must contain information

about how the boundary-layer transition location impacts the objective function.

2. Allowing the optimizer to manipulate the transition location through shape changes explores a design space that is unavailable to a fully turbulent approach. Previously studied airfoils such as the high lift-to-drag ratio airfoils produced by Zingg, and the maximum lift airfoils produced by Liebeck are unique to the laminar-turbulent design space.

3. The trade-offs associated between a fully turbulent design and laminar-turbulent design can be clearly captured through a weighted-sum Pareto front formulation. The information contained within the Pareto front can provide the designer with a clear picture of the trade-offs associated with different weightings on fully turbulent and laminar-turbulent conditions.

4. The Spalart-Allmaras turbulence model has the potential to create non-unique solutions when the solution is not initialized from free-stream. Therefore, when the transition point is variable, the solution should not be warm started from a previously converged solution.

A number of recommendations for future work are outlined in the area of aerodynamic shape optimization with laminar-turbulent transition:

- A significant drawback to the current algorithm is that the transition location is limited to the stream-wise spacing of the surface grid points. The consequence is that the optimizer is unable to achieve the optimum location for boundary-layer transition. Furthermore, since the grid consists of highly stretched cells along the surface of the airfoil, the transition location can jump from one station to the next with minor airfoil shape perturbations. This confuses the objective function and can lead to failed search directions. Allowing the trip location to exist in between grid nodes along the surface of the airfoil would remedy this situation

- MSES was used as a "stop-gap" measure in order to explore the challenges associated with airfoil shape optimization with transition prediction. An obvious improvement in the algorithm would be to replace MSES with a transition prediction routine based on the pressure distribution of the RANS solution. The implementation of the transition prediction can be fully coupled into the flow solver following the work of Stock et al. [49, 50, 51, 52] Using this approach the sensitivity of the objective function due to the movement of the transition location can be obtained through the adjoint method.

- An alternate approach to effectively designing airfoils that have a finite regions of laminar flow is using a turbulence model that automatically detects and models transitional flows.

The gradient will automatically contain information about how the movement of the transition location through shape changes will effect the objective function. A possible turbulence model that provides this capability can be found in the work of Langtry and Menter [25], Langtry et al. [26], and Menter et al. [34]. The transport equations that control the location and development of turbulence could be used to modify the Spalart-Allmaras model rather than the Menter SST model which they used.

References

[1] D. W. Banks, C. P. van Dam, H. J. Shui, and G. M. Miller, *Visualization of inflight flow phenomena using infared thermography*, Tech. Rep. TM-2000-209027, National Aeronautics and Space Administration (NASA), July 2000.

[2] R. D. Banner, J. G. McTigue, and G. Petty, *Boundary-layer-transition measurements in full-scale flight*, Tech. Rep. H58E28, National Advisory Committee for Aeronautics (NACA), Edwards, California, March 1958.

[3] P. Bradshaw, *Topics in Applied Physics: Turbulence (Second Corrected and Updated Edition) Vol. 12*, Springer-Verlag, Berlin Heidelberg New York, 1978.

[4] A. L. Braslow and F. Visconti, *Investigation of boundary-layer Reynolds number for transition on a NACA 65(215)-114 airfoil in the Langley two-dimensional low-turbulence pressure tunnel*, Tech. Rep. 1704, National Advisory Committee for Aeronautics (NACA), Langley Field, VA., Oct 1948.

[5] R. R. Brodeur and C. P. van Dam, *Transition prediction for a two dimensional Navier-Stokes solver applied to wind-turbine airfoils*, AIAA Paper 2000-0047, January 2000.

[6] W. K. Bullivant, *Tests of the NACA 0025 and 0035 airfoils in the full-scale wind tunnel*, Tech. Rep. 708, National Advisory Committee for Aeronautics (NACA), Langley Field, VA., September 1940.

[7] T. Chisholm and D. W. Zingg, *Start-up issues in a Newton-Krylov algorithm for turbulent aerodynamic flows*, AIAA Paper 2003-3708, June 2003.

[8] M. Clauser and F. Clauser, *The effect of curvature on the transition from laminar to turbulent boundary layer*, Tech. Rep. 613, National Advisory Committee for Aeronautics (NACA), Pasadena, CA, June 1937.

[9] S. S. Dodbele, *Design optimization of natural laminar flow bodies in compressible flow*, Tech. Rep. 4478, National Aeronautics and Space Administration (NASA), Langley Field, VA., 1993.

[10] M. Drela, *Design and optimization method for multi-element airfoils*, AIAA Paper 93–0969, 1993.

[11] M. Drela, *A User's Guide to MSES 2.95*, 1996.

[12] M. Drela and M. B. Giles, *Viscous-inviscid analysis of transonic and low Reynolds number airfoils*, AIAA Journal, 25 (1987), pp. 1347–1355.

[13] M. V. Dyke, *An Album of Fluid Motion*, The Parabolic Press, 1982.

[14] C. Gasley, *Boundary-layer stability and transition in subsonic and supersonic flow*, Journal of the Aeronautical Sciences, (1953), pp. 19–28.

[15] M. B. Giles and M. Drela, *Two-dimensional transonic aerodynamic design method*, AIAA Journal, 25 (1987), pp. 1199–1206.

[16] P. Godin, D. W. Zingg, and T. E. Nelson, *High-lift aerodynamic computations with one- and two-equation turbulence models*, AIAA Journal, 35 (1997), pp. 237–243.

[17] P. S. Granville, *The calculation of the viscous drag of bodies of revolution*, Tech. Rep. 849, Navy Department The David W. Taylor Model Basin, Washington 7, D.C., 1953.

[18] B. E. Green, J. L. Whitesides, R. L. Campbell, and R. E. Mineck, *A method for the constrained design of natural laminar flow airfoils*, AIAA Paper 96-2502, 1996.

[19] T. Herbert, *Boundary-layer transition analysis and prediction revisited*, AIAA Paper 91-0737, January 1991.

[20] J. Hua, P. J. Liu, and D. W. Zingg, *Optimization of long-endurance airfoils*, AIAA Paper 2003–3500, June 2003.

[21] F. G. B. J. R. Edwards, C. J. Roy and H. A. Hassan, *Development of a one-equation transition/turbulence model*, AIAA Journal, 39 (2001), pp. 1691–1698.

[22] A. Jameson, *Advances in aerodynamic shape optimization*, tech. rep., International Conference on Computational Fluid Dynamics (ICCFD) 3, Toronto, Canada, July 2004.

[23] R. D. Joslin, *Overview of laminar flow control*, Tech. Rep. NASA/TP-1998-208705, National Aeronautics and Space Administration (NASA), Langley Field, VA., October 1998.

[24] I. Kroo and P. Sturdza, *Design-oriented aerodynamic analysis for supersonic laminar flow wings*, AIAA Paper 2003-0774, January 2003.

[25] R. B. Langtry and F. R. Menter, *Transition modeling for general CFD applications in aeronautics*, AIAA Paper 2005-522, January 2005.

[26] R. B. Langtry, F. R. Menter, S. R. Likki, Y. B. Suzen, P. G. Huang, and S. Volker, *A correlation-based transition model using local variables part 2 - test cases and industrial applications*, ASME-GT2004-53454, ASME TURBO EXPO 2004, Vienna, Austria, 2004.

[27] R. H. Liebeck, *A class of airfoils designed for high lift in incompressible flow*, Journal of Aircraft, 10 (1973), pp. 610–617.

[28] H. W. Liepmann and G. H. Fila, *Investigations of effects of surface temperature and single roughness elements on boundary-layer transition*, Tech. Rep. 1196, National Advisory Committee for Aeronautics (NACA), Pasadena, CA, August 1946.

[29] J. Liu, *Comparison of Optimization Algorithms Applied to Aerodynamic Design*, Master's thesis, University of Toronto, 2003.

[30] H. Lomax, T. H. Pulliam, and D. W. Zingg, *Fundamentals of Computational Fluid Dynamics*, Springer–Verlag, Berlin, Heidelberg, 2001.

[31] R. W. MacCormack, *A perspective on a quarter century of CFD research*, AIAA Paper 93–3291, July 1993.

[32] R. J. McGhee and W. D. Beasley, *Low-speed aerodynamic characteristic of a 17-percent-think airfoil section designed for general aviation applications*, Tech. Rep. TN D-7428, National Aeronautics and Space Administration (NASA), Langley Field, VA., December 1973.

[33] F. R. Menter, *Zonal two-equation k-w models for aerodynamic flows*, AIAA Paper 93-2906, July 1993.

[34] F. R. Menter, R. B. Langtry, S. R. Likki, Y. B. Suzen, P. G. Huang, and S. Volker, *A correlation-based transition model using local variables part 1 - model formulation*, ASME-GT2004-53452, ASME TURBO EXPO 2004, Vienna, Austria, 2004.

[35] T. E. Nelson and D. W. Zingg, *Fifty years of aerodynamics: Successes, challenges, and opportunities*, CAS Journal, 50 (2004), pp. 61–84.

[36] M. Nemec, *Optimal Shape Design of Aerodynamic Configurations:A Newton-Krylov Approach*, PhD thesis, University of Toronto, 2003.

[37] M. Nemec and D. W. Zingg, *Newton–Krylov algorithm for aerodynamic design using the Navier–Stokes equations*, AIAA Journal, 40 (2002), pp. 1146–1154.

[38] M. Nemec and D. W. Zingg, *Optimization of high-lift configurations using a Newton-Krylov algorithm*, AIAA Paper 2003-3957, 2003.

[39] Nihon University Aero Student Group, *NASG airfoil database*, tech. rep., http://www.nasg.com/afdb/show-airfoil-e.phtml?id=826, 2005.

[40] J. Pralits, *Optimal Design of Natural and Hyrbid Laminar Flow Control on Wings*, PhD thesis, Royal Institute of Technology Department of Mechanics, Stockholm, Sweden, October 2003.

[41] A. Pueyo, *An Efficient Newton–Krylov Method for the Euler and Navier–Stokes Equations*, PhD thesis, University of Toronto, 1998.

[42] T. H. Pulliam, *Efficient solution methods for the Navier-Stokes equations*, tech. rep., Lecture Notes for the von Kármán Inst. for Fluid Dynamics Lecture Series: Numerical Techniques for Viscous Flow Computation in Turbomachinery Bladings, Brussels, Belgium, Jan 1986.

[43] H. L. Reed, T. S. Haynes, and W. S. Saric, *Computational fluid dynamics validation issues in transition modeling*, AIAA Journal, 36 (1998), pp. 742–751.

[44] H. Schlichting, *Boundary-Layer Theory, 6th edn.*, McGraw-Hill, New York, 1979.

[45] G. B. Schubauer and P. S. Klebanoff, *Contributions on the mechanics of boundary-layer transition*, Tech. Rep. 1289, National Advisory Committee for Aeronautics (NACA), Washington, D.C., February 1955.

[46] A. Silverstein and J. V. Becker, *Determination of boundary-layer transition on three symmetrical airfoils in the NACA full-scale wing tunnel*, Tech. Rep. 637, National Advisory Committee for Aeronautics (NACA), Langley Field, VA., May 1938.

[47] A. M. O. Smith and N. Gamberoni, *Transition, pressure gradient and stability theory*, Tech. Rep. ES 26388, Douglas Aircraft Co., Long Beach, CA, 1956.

[48] P. R. Spalart and S. R. Allmaras, *A one-equation turbulence model for aerodynamic flows*, AIAA Paper 92–0439, Jan. 1992.

[49] H. W. Stock, *Airfoil validation using coupled Navier-Stokes and e^n transition prediction methods*, Journal of Aircraft, 39 (2002), pp. 51–58.

[50] H. W. Stock and W. Haase, *Feasibility study of e^N transition prediction in Navier-Sokes methods for airfoils*, AIAA Journal, 37 (1999), pp. 1187–1196.

[51] ——, *Navier-Stokes airfoil computations with e^n transition prediction including transitional flow regions*, AIAA Journal, 38 (2000), pp. 2059–2066.

[52] H. W. Stock and A. Seitz, *Crossflow-induced transition prediction using coupled Navier-Stokes and e^n method computations*, AIAA Journal, 42 (2004), pp. 1746–1754.

[53] P. Sturdza, *An Aerodynamic Design Method for Supersonic Natural Laminar Flow Aircraft*, PhD thesis, Stanford University, 2003.

[54] Y. B. Suzen and P. G. Huang, *Modeling of flow transition using an intermittency transport equation*, Journal of Fluids Engineering, 122 (2000), pp. 273–284.

[55] J. L. van Ingen, *A suggested semi-empirical method for the calculation of the boundary layer transition region*, Tech. Rep. VTH-74, Dept. of Aerospace Engineering, University of Delft, Delft, The Netherlands, 1956.

[56] A. E. von Doenhoff, *A preliminary investigation of boundary-layer transition along a flat plate with adverse pressure gradient*, Tech. Rep. 639, National Advisory Committee for Aeronautics (NACA), Langley Field, VA., March 1938.

[57] E. S. Warren and H. A. Hassan, *Transiton closure model for predicting transition onset*, Journal of Aircraft, 35 (1998), pp. 769–775.

[58] E. W. Warren and H. A. Hassan, *Alternative to the e^n method for determining onset of transition*, AIAA Journal, 36 (1997), pp. 111–113.

[59] F. M. White, *Fluid Mechanics, 4th ed.*, McGraw-Hill, New York, 1999.

[60] A. R. Wilkinson and D. W. Zingg, *AMBER 2d User's Guide*, 1993.

[61] P. Wong, *Aerodynamic Optimization Using the Flow Sensitivity Approach*, Master's thesis, University of Toronto, 2001.

[62] T. W. Young, E. S. Warren, J. E. Harris, and H. A. Hassan, *New approach for the calculation of transitional flows*, AIAA Journal, 31 (1993), pp. 629–636.

[63] D. W. Zingg, *An Approach to the Design of Airfoils With High Lift to Drag Ratios*, Master's thesis, University of Toronto, 1981.

[64] D. W. Zingg, S. De Rango, and A. Pueyo, *Advances in algorithms for computing aerodynamics flows*, in Frontiers of Computational Fluid Dynamics 2002, D. A. Caughey and M. M. Hafez, eds., Singapore, 2002, World Scientific.